Physics of Plasmas

Edge turbulence velocity preceding the L-H transition in NSTX

Cite as: Phys. Plasmas **28**, 032304 (2021); https://doi.org/10.1063/5.0039153
Submitted: 01 December 2020 . Accepted: 23 February 2021 . Published Online: 19 March 2021

S. J. Zweben, A. Diallo, M. Lampert, T. Stoltzfus-Dueck, and S. Banerjee

Physics of Plasmas ARTICLE scitation.org/journal/php

Edge turbulence velocity preceding the L-H transition in NSTX

Cite as: Phys. Plasmas **28**, 032304 (2021); doi: 10.1063/5.0039153
Submitted: 1 December 2020 · Accepted: 23 February 2021 ·
Published Online: 19 March 2021

S. J. Zweben,[1,a)] A. Diallo,[1] M. Lampert,[1] T. Stoltzfus-Dueck,[1] and S. Banerjee[2]

AFFILIATIONS

[1]Princeton Plasma Physics Laboratory, Princeton, New Jersey, USA
[2]College of William and Mary, Williamsburg, Virginia, USA

[a)]Author to whom correspondence should be addressed: stewart.zweben@gmail.com

ABSTRACT

The low-to-high mode or L-H transition in tokamaks involves a sudden reduction in the edge turbulence level and a decrease in the edge plasma transport. The mechanism for the L-H transition is widely believed to be associated with changes in the poloidally averaged poloidal turbulence velocity. Using a gas puff imaging (GPI) diagnostic, the poloidally averaged poloidal turbulence velocity $\langle V_{pol}\rangle_{pol}$ was measured for a set of 16 shots with L-H transitions in NSTX. These measurements were focused −2 cm inside the separatrix where the relative fluctuation level as seen in GPI decreases significantly and consistently at the transition. The magnitude of this poloidal velocity preceding the transition varied widely, ranging from $|V_{pol}| \sim 1$–4 km/s during the last 1 ms before the transition, and the magnitude of the radial gradient also had a wide shot-to-shot range of $|\text{grad } V_{pol}| \sim 0.34$ to 1.9 km/s cm during this same time. The frequency spectrum of $\langle V_{pol}\rangle_{pol}$ during the 30 ms before the transition had a near-coherent peak at ∼2–5 kHz, but only in about half of these shots. In general, there were no clear and consistent changes in the poloidal velocity of the turbulence preceding the L-H transition in this database.

I. INTRODUCTION

A sudden transition from low-to-high confinement plasmas or "L-H transition" has been observed in tokamaks for many years,[1] but is not yet completely understood. The H-mode confinement state is important since it appears to be necessary to obtain ignition in ITER and future tokamaks. The goal of this paper is to better understand the triggering mechanism for this L-H transition by analyzing measurements of the turbulence velocity and turbulence velocity shear preceding the transition in the spherical tokamak NSTX.

Over the past 35+ years, extensive theoretical research has produced a diverse group of models for the L-H transition, involving mechanisms such as stability thresholds, neoclassical effects, and the influence of the scrape-off layer or divertor region.[1,2] The most popular models focus on the effects of the characteristic edge electric field well, especially on the possible role of electric field shear in suppressing plasma turbulence.[3] If the zonal (poloidally averaged) electric field or its shear (radial derivative) are causal for the L-H transition, it seems likely that the L-H transition should be preceded by some reproducible pattern of zonal electric field evolution. Since the perpendicular velocity of the edge plasma is usually dominated by the E × B drift, this reproducible pattern should also be detectible in the cross-field velocities of the edge plasma, closely related to the velocity inferred from velocimetry applied to imaging of edge turbulence.

In this paper, we examine gas puff imaging (GPI) movies of edge turbulence in search of consistent changes in the turbulence velocity or turbulence velocity shear preceding the L-H transition in NSTX. Although the GPI diagnostic does not directly measure the radial electric field or plasma flow velocity, it does give information concerning the motion of the turbulence itself, which ought to be relevant for understanding the basic mechanism of turbulence suppression and improved confinement at the L-H transition.

There is an extensive literature on turbulence measurements across the L-H transition, including several recent review papers.[4–8] The key background issue for this paper is whether there are consistent changes in the turbulence velocity just before the L-H transition. If so, then these changes can then be understood as the cause of the transition, at least within the context of a specific model.

This paper is an extension of two previous papers about the L-H transition as measured by the GPI diagnostic on NSTX. The first of these[9] used GPI data from 2009 with a 64 × 64 pixel resolution and a framing rate of 121 000–285 000 frames/s. That paper focused on a correlation between quiet periods of low GPI fluctuation level and the oscillating poloidal velocity of the edge turbulence preceding the L-H

transition. The poloidally averaged poloidal velocity was evaluated using a cross correlation method similar to that in this paper, which showed no systematic velocity or velocity shear variations before the transition. The second paper[10] used improved GPI data from 2010 with a new camera having 64 × 80 pixel resolution at a higher framing rate of 400 000 frames/s and examined the local energy exchange dynamics during the L-H transition. This paper uses the same GPI data as the second paper but focuses on a more systematic and detailed analysis of the poloidal turbulence velocity and its time and frequency variations preceding the L-H transition.

In general, plasma turbulence velocity measurements are difficult because the local velocity can vary significantly in magnitude and direction on the space and timescales of the turbulence, i.e., a few cm and a few microseconds. Thus the plasma turbulence in a given region does not have a single precise velocity like a rigid body, but moves more like a turbulent cloud in the sky. The turbulence velocity in this paper is defined by a time-delayed cross correlation algorithm described in Sec. II C and in the Appendix. This paper focuses on the poloidally averaged poloidal velocity within the GPI field of view, which is closely related to the edge radial electric field and zonal flow.[11]

There have been many previous measurements of the edge turbulence velocity preceding the L-H transition in toroidal magnetic fusion devices. The following three paragraphs review some of these results, focusing on relatively recent tokamak experiments (other references can be found in the review articles cited above). Note that optical diagnostics such as GPI and microwave reflectometry measure the velocity of turbulent perturbations in the poloidal direction (including the poloidal component of the toroidal velocity), while Langmuir probes measure the radial electric field E_r, which determines the poloidal $E_r \times B$ fluid velocity.

Poloidal velocity measurements of the turbulence before the L-H transition in DIII-D have been made using BES (beam emission spectroscopy), a 2-D imaging diagnostic similar to GPI. A slow increase in poloidal velocity was observed within ∼10 ms before the transition,[12,13] with an added increase 0.1 ms before the transition in one case. On the other hand, a quasi-periodic 1–2 kHz oscillation in the poloidal turbulence velocity was seen using GPI during the ∼15 ms preceding an L-H transition in EAST,[14] while only a single sudden increase in the poloidal turbulence velocity was observed with GPI within ∼1 ms of the transition in Alcator C-Mod.[15]

Large oscillations in the edge poloidal velocity have been observed using Doppler reflectometry in the intermediate phase between the L- and H-modes, for example, at ∼2–3 kHz in ASDEX Upgrade[16] and DIII-D.[17] More recently, these oscillations were sometimes seen on ASDEX Upgrade to transition smoothly into intermittent bursts similar to type-III edge localized modes (ELMs).[18] Stationary zonal flows (i.e., at zero frequency) have also been measured using reflectometry in JET,[19] and oscillatory flows were seen to change into mean flows just prior to the L-H transition in the HL-2A tokamak.[20]

Langmuir probe measurements on the EAST tokamak also showed quasi-periodic E_r oscillations and poloidal flows preceding the L-H transition, but sometimes showed more broadband and intermittent features.[21,22] In a recent paper by the same group,[23] small-amplitude oscillations were seen before the L-H transition which increased the turbulence level and amplitude of the zonal flow. In HL-2A, an increasing E_r during the intermediate phase was accompanied by an increase in inward turbulent particle transport.[24]

Qualitatively similar results on the L-H transition have been obtained on stellarators.[1,7] For example, the spatiotemporal structure of turbulence and oscillating poloidal flows at the transition have been measured using reflectometry in TJ-II,[25] and the dependence of the low-frequency zonal flows on the plasma heating scenario have been measured using floating potential probes on the same device.[26] This similarity between stellarators and tokamaks suggests that the L-H transition is a general feature of toroidal magnetic devices.

This paper on NSTX contains a study of the turbulence velocity preceding the L-H transition using a relatively large database compared with these previous results, which generally had only a few shots per paper. These present results were centered at –2 cm inside the separatrix near the outer midplane where the relative turbulence level decreases significantly and consistently at the transition, which is also near to where most of the measurements cited above were made. The time period examined here is up to 15 ms before the transition, which is the same time range over which velocity changes were seen in the previous papers. A special focus is given here to the 1 ms period before the transition.

The overall conclusion of this study is that that was no consistent time variation of the poloidal turbulence velocity preceding the L-H transition in this NSTX database. The most striking result was the large shot-to-shot variability, which is reminiscent of the large variability seen in the other devices cited above. For example, during the last 1 ms before the transition the poloidal velocity ranged from $|V_{pol}|$ ∼1–4 km/s and its radial gradient ranged from|grad V_{pol} | ∼0.34 to 1.9 km/s cm, with oscillating poloidal flows in only about half of the shots. Thus there was no clear and consistent cause for the L-H transition identified from this poloidal turbulence velocity analysis.

This paper is organized as follows: Sec. II describes the diagnostics, database, and analysis method. Sec. III describes the experimental results. Sec. IV contains a Discussion.

II. DIAGNOSTICS, DATABASE, AND ANALYSIS METHOD

This paper describes an analysis of the edge turbulence velocity based on GPI data from the 2010 run of NSTX. The database of shots is the same as in a previous paper,[10] but the focus here is on the poloidally averaged turbulence velocity rather than the local energy exchange dynamics. Here we also focus on the time period *preceding* the L-H transition, and do not attempt to compare the turbulence velocities before the transition with those found in H-mode after the transition. This is partly due to GPI diagnostic limitations, since the radial extent of the GPI signal is significantly reduced in H-mode, and the velocity calculations are more uncertain in the near-quiescent H-mode period. Unfortunately, there were no other fast (kHz) diagnostics of edge plasma velocity, density, or temperature in NSTX during this run period.

A. GPI diagnostic

The NSTX GPI diagnostic has been described previously [e.g., 27], so only a brief summary is presented here. In GPI, a fast camera (Vision Research Phantom 710) views an injected deuterium neutral gas puff in order to make 2D images of its neutral deuterium line emission. The camera views the plasma through a Dα filter (656 ± 4.5 nm FWHM), and its view is as near as possible aligned along the local

magnetic field just above the outer midplane separatrix. This creates images of the local Dα light emission from the gas cloud which covers about 24 cm radially (i.e., perpendicular to the local separatrix) vs 30 cm poloidally (i.e., along the local separatrix) with 64 × 80 pixels taken at 400 000 frames/s (2.5 μs/frame). For calculating the relative fluctuation level (but not the turbulence velocity), the original image is smoothed over ±1 pixel or ±0.38 cm, which is smaller than the optical resolution of ∼1 cm.

Most of this GPI light emission in NSTX occurs within ±5–10 cm of the separatrix in the region where the electron temperature is high enough to excite the Dα line, but low enough so that the neutrals are not completely ionized, typically within Te ∼ 10–200 eV.[28] The Dα light emission seen in GPI fluctuates due to the local electron density and temperature perturbations. Various issues and assumptions in the interpretation of these GPI images were discussed in a recent diagnostic review paper.[29] The present analysis is done using Dα light emission images with no attempt to unfold the underlying electron density fluctuations.

The GPI puff introduces deuterium gas into the edge plasma, and this can cause a small increase in the edge density and decrease in the edge electron temperature in Ohmic plasmas, as described previously.[30] However, as far as we know the GPI gas puff had no significant effect on the turbulence or the L-H transitions in these shots. Since the GPI gas puff timing was preprogramed before the shot and the exact L-H transition time was not predictable, the transition in these shots occurred from 2 to 42 ms after the peak of the GPI signal level. The GPI signal level at the transition varied by a factor of 5 from shot-to-shot, but its value changed by an average of only ∼25% during the 15 ms preceding these L-H transitions.

B. Database

The 16 shots used in this paper are listed in Table I. These are the same shots used in a previous paper on the energy exchange dynamics in the L-H transition,[10] but one of those shots (#141745) was removed because the separatrix location was too close to the edge of the GPI image for the present analysis. All shots had a moderate toroidal field for NSTX of $B_t = 3.6$–4.4 kG, a moderate plasma current $I_p = 800$–910 kA, and a lower single null divertor geometry with the magnetic axis at $R = 98 \pm 3$ cm. These 16 shots are representative of the range of L-H transitions seen in NSTX. All shots were made with deuterium fueling and the NBI heating and fueling was deuterium.

Most shots had an outer midplane separatrix radius at Rsep = 148–149 cm at the transition time (as determined by EFIT02), but some had Rsep = 152–154 cm for better RF coupling. All the L-H transitions in these shots occurred at least 5 ms after the current flattop, which began at ∼0.2 s (the typical timescale for current diffusion in the NSTX L-mode edge is a few millisecond). Nine of the 16 shots had low power ($P \leq 1.4$ MW) auxiliary heating at the L-H transition time, and seven shots had the L-H transitions in Ohmic plasmas. Three shots had the transitions occurring ≤20 ms after the start of NBI heating (#138113, 138114, 138119), two shots had the transitions occurring ≥100 ms after the start of NBI (#139955, 142229), and the four RF shots had the transitions occurring ∼20–40 ms after the start of RF heating. All shots showed the usual sharp drop in the Dα emission at the L-H transition, along with a sharp drop in the relative edge fluctuation level as seen by GPI.

In this paper the time before the L-H transition will be called "L-mode" even though the plasmas were Ohmic with no auxiliary power. Movies of the GPI image data can be found in the supplementary material for this paper or in Ref. 31.

C. Data analysis

The analysis of turbulence velocity in this paper is done with the GPIFLOW code, which is described in detail in the Appendix. This is essentially the same code used for a small part of a previous paper on energy exchange dynamics at the L-H transition in NSTX,[10] and also

TABLE I. Shot list.

Shot #	Bt (kG)	Ip (kA)	Rsep (cm)	Peak GPI time (ms)	L-H time (ms)	P (MW) at L-H	$\lvert V_{pol}\rvert$ (km/s)[a]	$\lvert \text{grad } V_{pol}\rvert$ (km/s cm)[a]
138113	4.4	910	149	226	254.9	1.4 NBI	3.66	1.26
138114	4.4	910	149	226	252.5	1.4 NBI	1.79	0.62
138115	4.4	910	149	226	243.0	0	2.59	1.38
138116	4.4	910	149	226	251.6	0	2.56	1.36
138117	4.4	910	148	226	245.8	0	3.40	1.13
138118	4.4	910	148	226	249.5	0	2.84	0.78
138119	4.4	910	149	226	268.4	1.2 NBI	4.00	1.16
139955	4.4	900	148	362	364.3	1.0 NBI	3.82	0.34
141746	3.6	800	149	212	244.9	0	3.42	1.68
141747	3.6	800	148	212	226.5	0	2.53	1.65
141751	3.6	800	149	212	235.0	0	2.77	1.89
141919	4.4	910	154	205	231.1	0.6 RF	1.29	1.05
141920	4.4	910	154	213	241.5	0.6 RF	0.99	1.58
141922	4.4	910	154	213	237.5	0.7 RF	1.95	1.59
142006	4.4	910	154	220	223.0	0.5 RF	2.33	1.01
142229	4.4	800	152	382	401.8	1.0 NBI	3.34	0.51

[a]Averaged over −1.1 to −0.1 ms before the L-H transition.

for earlier papers on analysis of zonal flows in GPI data from NSTX[9] and Alcator C-Mod.[32]

The GPIFLOW algorithm is based on the intuitive idea that the turbulence flow velocity can be estimated by cross-correlating a short time series from a given pixel in the 2D image with time-delayed time series at all neighboring pixels. The location of the maximum of this time-delayed cross correlation is used to determine the movement of the turbulence in the GPI image plane, i.e., the 2D velocity is evaluated from the displacement of the maximum of this time-delayed correlation over a single time frame. Note that this analysis does not attempt to identify any individual "blob" structures in the image data, but uses normalized cross correlation functions of the unfiltered time series of GPI image pixels. This is a simple and intuitive method of velocimetry which makes no assumptions about the nature of the flow. This code does not use the same algorithm as previous codes used for velocimetry of GPI[14,33–35] or BES.[36–38] A comparison of this algorithm and a Fourier velocimetry method was given in Ref. 39.

The focus of analysis in this paper is on the low frequency poloidally averaged poloidal flow velocities, which we write "$\langle V_{\mathrm{pol}}\rangle_{\mathrm{pol}}$." This is as close as this diagnostic allows to a measurement of the zonal flow velocity, since the averaging extend over several poloidal wavelengths. Such zonal flows have previously been seen in NSTX[9,32] and in many other magnetic fusion experiments.[11] The poloidal averaging is limited to 21 cm due to the GPI geometry, and the analysis radius is focused on -2 ± 1 cm inside the local separatrix. The flow velocity analysis is also limited to the low-frequency range below 20 kHz by the cross correlation process, and to velocities below 15 km/s by the search algorithm. Further description of the GPIFLOW algorithm is presented in Sec. IV B and the Appendix.

III. EXPERIMENTAL RESULTS

The experimental results for turbulence velocities are presented in this section. Since there is a significant shot-to-shot variation in these results, we first describe a few specific examples in detail, and then discuss the wider database of all 16 shots (Table I). For the sake of clarity, an overview of these experimental results is presented in the following three paragraphs.

The first example as described in Sec. III A was chosen to be a shot in which the L-H transition occurred shortly after the start of NBI (#138113). Figures 1–3 present a description of the GPI signals vs time across the transition, and then Figs. 4 and 5 describe the poloidal velocity analysis. This shot had a near-coherent oscillation in the poloidally averaged poloidal velocity preceding the transition (i.e., a zonal flow), which was seen in about half the shots in this database. The second example as described in Sec. III B and Figs. 6–10 was a shot in which the L-H transition occurred shortly after the start of RF heating (#141922). However, this shot did *not* have a clear coherent oscillation in the poloidal velocity preceding the transition, and so demonstrates that this feature is not necessary for an L-H transition in NSTX.

Three other individual shots are then described more briefly in Sec. III C; namely, one shot with a transition in a purely Ohmic plasma (#141751), one shot with a transition during RF heating (#142006), and one shot in which the transition occurred at $\geq$100 ms after the start of NBI (#142229). These poloidally averaged poloidal velocities vs time and their frequency spectra are shown in Fig. 11. Section III D discusses the estimation of poloidal velocity shear calculated from the radial gradient of the poloidally averaged poloidal velocity, as shown in Fig. 12. This velocity shear is important in some theories of the L-H transition.

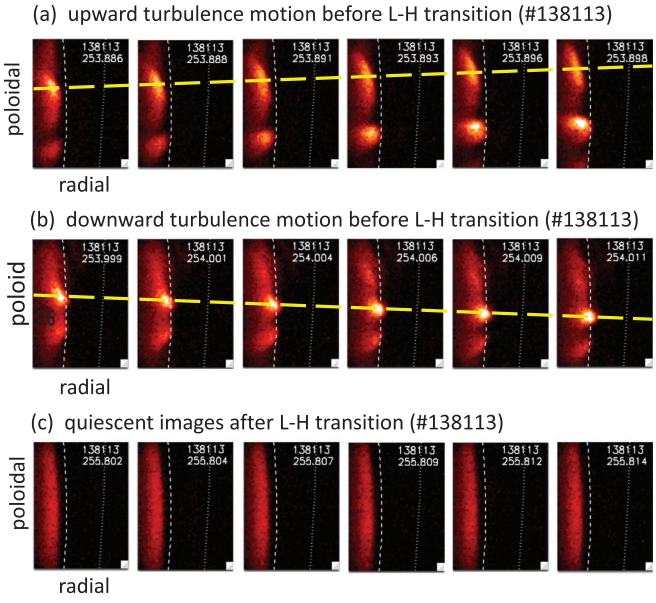

FIG. 1. A series of frames of raw GPI data from shot #138113. Each part (a)–(c) has six successive frames separated by 2.5 μs. The frames in (a) show an upward poloidal turbulence motion (electron diamagnetic direction), the frames in (b) show a downward poloidal turbulence motion about 100 μs after (a), both in L-mode. The motion of sample turbulent structures is indicated by the yellow dashed line. The frames in (c) were about 1 ms after the L-H transition and show a quiescent H-mode state with little turbulence structure or motion.

The wider database results are presented in Secs. III E and III F, with Sec. III E focusing on the poloidal velocity and Sec. III F on the frequency spectrum of the poloidal velocity. The aim of these sections is to search for consistent changes in the poloidal turbulence velocity preceding the L-H transition. First, Fig. 13 shows the shot-averaged values vs time of the relative GPI fluctuation level, the magnitude the poloidal velocity, and the magnitude of the radial gradient of the poloidal velocity. Then, Fig. 14 shows poloidal velocity results for each of the 16 individual shots, and finally Fig. 15 shows frequency spectrum results for these shots.

A. First example: #138113

This first example had an L-H transition which occurred in shot #138113 at $\leq$10 ms after the start of 1.4 MW of NBI in a plasma with $I = 0.9$ MA and $B = 4.4$ kG (see Table I). After the transition a large density pedestal and edge density gradient forms just inside the outer midplane separatrix, as usual for H-modes in NSTX.[40,41]

Figure 1 shows a series of frames of raw GPI data from shot #138113. Each frame has 64 × 80 pixels and covers 24 cm radially (i.e., horizontal) by 30 cm poloidal (vertical), with the separatrix shown as a dashed line and the limiter (RF antenna) shadow to the right shown as a dotted line. In this paper, the local poloidal direction is assumed to be vertical in each image (here poloidal means binormal, i.e., in the flux surface but perpendicular to B), and the local radial direction is

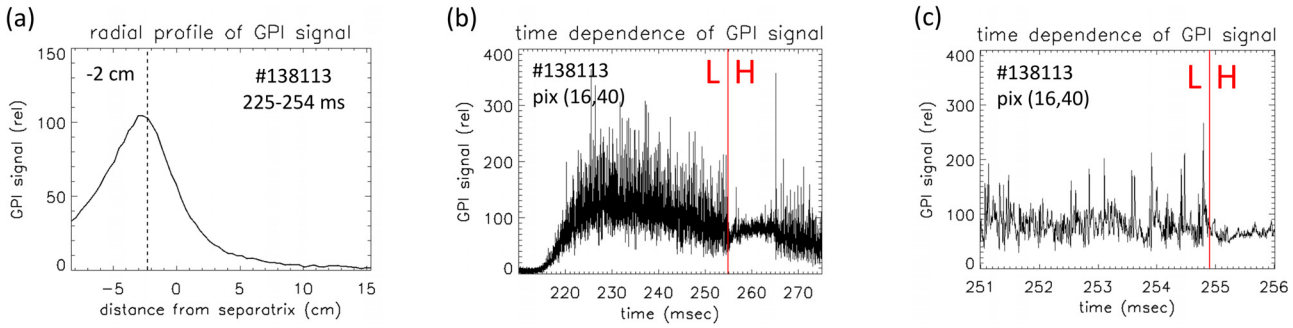

FIG. 2. Examples of GPI signals for shot #138113. In (a) is the radial profile of the signal amplitude before the L-H transition showing the signal level peaking at –2 cm inside the separatrix. In (b) is the time dependence of the GPI signal at a single pixel, and in (c) is the same signal on a faster timescale near the transition (red line). The relative fluctuation level decreases significantly at the transition.

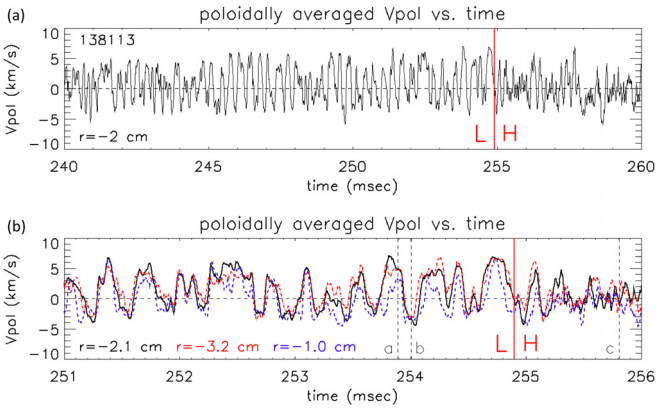

FIG. 3. Poloidally averaged poloidal velocity $\langle V_{pol}\rangle_{pol}$ vs time at a radius of –2 cm for shot #138113. Part (a) shows near-coherent oscillations with a maximum amplitude of ±5 km/s during the 15 ms before the L-H transition. The same signal is shown in black in (b) over 5 ms near the L-H transition, and overlaid with similar signals from radii of –3 cm and –1 cm. The times of the images in Fig. 1 are shown as the vertical dashed lines (a)–(c). A positive $\langle V_{pol}\rangle_{pol}$ is in the electron diamagnetic direction.

assumed to be horizontal. More about the geometry of GPI in NSTX can be found in Ref. 27.

Each part of Figs. 1(a)–1(c) has six successive frames separated by 2.5 μs. The frames in (a) were chosen to illustrate an upward poloidal turbulence motion (electron diamagnetic direction) which occurred ~1 ms before the L-H transition, the frames in (b) were chosen to illustrate a downward poloidal turbulence motion (ion diamagnetic direction) which occurred about 100 μs after (a) and 0.9 ms before the L-H transition. The motion of sample turbulent structures is indicated by the yellow dashed line. Comparing (a) and (b), the turbulence changed its poloidal direction in about 100 μs, and in both cases had a poloidal velocity ~1/6 (30 cm)/12.5 μs ~4 km/s. Note that the structures visible in (a) and (b) are all inside the separatrix, indicating that they are part of the turbulence spectrum and not "blobs," which exist only outside the separatrix.

The frames in Fig. 1(c) were taken about 1 ms *after* the L-H transition and show a narrow radial profile with little turbulence structure or motion indicating a relatively quiescent H-mode state, as seen previously in NSTX GPI data.[28] A similar narrow profile during H-mode was previously shown to be consistent with the expected Dα emission profile in the steep density gradient region.[42]

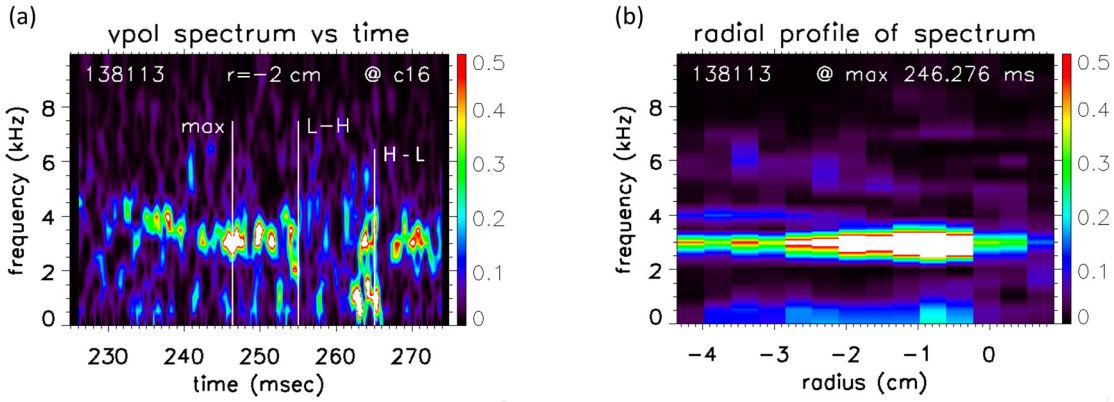

FIG. 4. In (a) is the power spectrum of $\langle V_{pol}\rangle_{pol}$ fluctuations at a radius of –2 cm as a function of frequency and time. There is a nearly coherent 3–4 kHz zonal flow oscillation over ~20 ms preceding the L-H transition, with maximum spectral power at 8 ms before the L-H transition. In (b) is the radial profile of the $\langle V_{pol}\rangle_{pol}$ power spectrum at the time of the maximum spectral power in (a). The frequency of the zonal flow spectrum at this time is ~3 kHz over the radial range of –4 cm to 0 cm inside the separatrix.

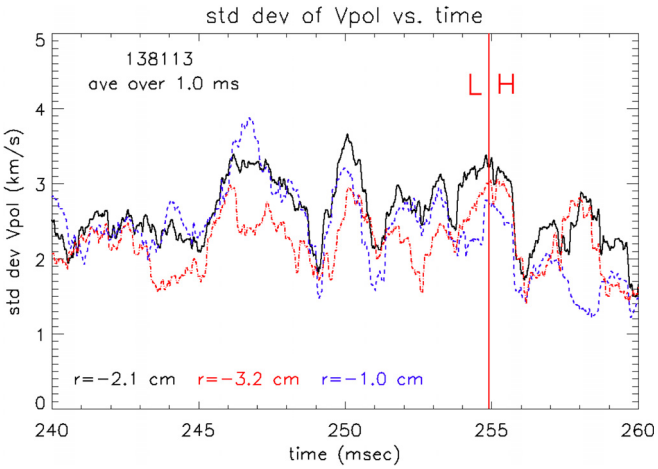

FIG. 5. The fluctuation level (standard deviation) of the $\langle V_{pol}\rangle_{pol}$ velocity vs time at three radii just inside the separatrix for shot #138113. The time-average is taken over 1 ms preceding each time point. There is no significant increase in the fluctuation level during the last 1 ms before the transition, compared with the 10 ms period before the L-H transition.

Before describing the turbulence velocity results, we show some GPI signals for this shot. In Fig. 2(a) is the average radial profile of the GPI signal amplitude before the L-H transition (225–254 ms), where the horizontal coordinate is the distance from the local separatrix as measured at row #40/80, and the vertical scale is the average GPI signal over rows #10–69. The GPI signal peaks about −2 cm inside the separatrix, which is where the poloidal velocity will be evaluated. Figure 2(b) shows the time dependence of the GPI signal at a radius of −2 cm and poloidally at the vertical center of the image (column #16, row #40), after smoothing over ±1 pixel, and beginning just before

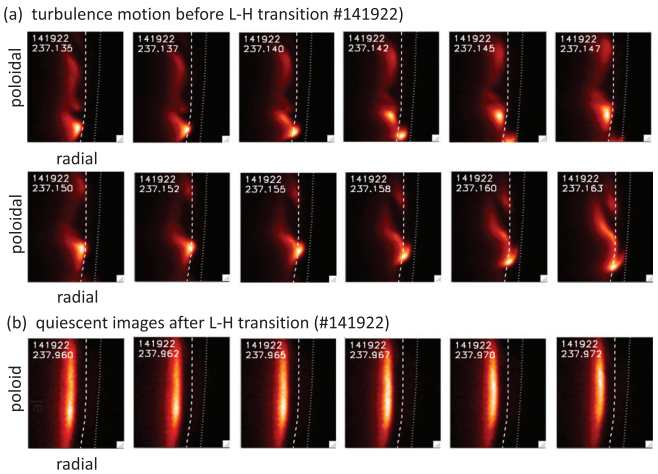

FIG. 6. A series of frames of raw GPI data from shot #141922. Part (a) has 12 successive frames separated by 2.5 μs at 0.4 ms before the L-H transition. These images show the complex turbulence structure and motion in this shot, with no clear poloidal velocity oscillations as in Fig. 1. The frames in Fig. 6(b) were taken about 0.4 ms after the L-H transition and show a narrow radial profile with relatively little turbulence structure or motion, indicating a quiescent H-mode state as in Fig. 1(c).

the GPI gas puff starts at 215 ms. The relative fluctuation level decreases significantly at the L-H transition time of 254.9 ms, as shown by the red line, and then goes back up about 10 ms later at an H-L transition. Figure 2(c) shows the L-H transition with higher time resolution. The time of the L-H transition shown by the red line, at which the relative fluctuation level decreases over a period of about ±100 μs. This decrease in the relative edge fluctuation level is a universal characteristic of the L-H transition, as seen previously in NSTX[10] and other tokamaks.

The turbulence velocity results below were obtained from the GPIFLOW code, which is described in detail in the Appendix. The goal of this code was to estimate the poloidally averaged poloidal turbulence velocity, which is as close as this diagnostic can provide to an estimate of the zonal flow. The code assumes that the image rows vs columns are aligned in the poloidal vs radial direction (see Fig. 1). The first step was to calculate the 2-D turbulence velocity at a single pixel using a time-delayed cross correlation function averaged over ±11 frames or ±27.5 μs around each time frame. The time delay was chosen to be 1 frame for this analysis. The poloidal turbulence velocity was then averaged over 15 different pixels in each image column spaced 4 rows (1.5 cm) apart, i.e., over 21.5 cm. The result was the poloidally averaged turbulence velocity at each radius. The poloidal velocity at these 15 poloidal locations was highly correlated, as illustrated in Fig. 4 of Ref. 10. This poloidally averaged poloidal turbulence velocity was then calculated for every time frame from 30 ms before to 20 ms after the L-H transition. This local poloidal (i.e., binormal) average velocity is called "$\langle V_{pol}\rangle_{pol}$" in the discussion below.

Figure 3(a) shows the poloidally averaged poloidal velocity $\langle V_{pol}\rangle_{pol}$ vs time for the GPI column nearest the radius −2 cm for shot #138113 (column #16). During the 15 ms period before the L-H transition, this velocity has some near-coherent oscillations at a frequency of ~3 kHz and a maximum amplitude of about ±5 km/s, with less coherent and smaller amplitude fluctuations during the 5 ms after the L-H transition. A positive $\langle V_{pol}\rangle_{pol}$ is in the electron diamagnetic direction, which corresponds to a negative E_r.

This same $\langle V_{pol}\rangle_{pol}$ signal is shown in black in Fig. 3(b) over a period of 5 ms near the L-H transition, and overlaid with $\langle V_{pol}\rangle_{pol}$ signals at radii of −3 and −1 cm (i.e., columns #13 and 19). The $\langle V_{pol}\rangle_{pol}$ signals at all three radii have approximately (but not exactly) the same time dependence. The times of the images of Fig. 1 are shown in Fig. 3(b) as vertical dashed lines labeled (a), (b), and (c), where (a) has an upward (positive) velocity, (b) has a downward (negative) velocity 100 μs later, both during the L-mode period, and (c) is in H-mode about 1 ms after the L-H transition.

Figure 4(a) shows the power spectrum of $\langle V_{pol}\rangle_{pol}$ as a function of time, i.e., the square of the $\langle V_{pol}\rangle_{pol}$ amplitude vs frequency for the column nearest $r = -2$ cm (#16). These spectra were calculated using a moving time interval of ± 1 ms (±400 frames) with a frequency resolution of 0.5 kHz up to 20 kHz (only 0–10 kHz is shown). The color scale at the right shows the relative magnitude of these fluctuations from 0 (black) to 0.5 (white). There is a nearly coherent zonal flow-like oscillation at 3–4 kHz during the 20 ms before the L-H transition. This is not a continuous mode, but has a bursting character, as seen previously (using a different type of velocimetry) during an L-mode shot from the 2009 NSTX run.[34] This is unlike a quasi-coherent mode moving at constant poloidal velocity, such as seen at ~40 kHz in Ohmic NSTX GPI data,[43] and these zonal flow oscillations have not

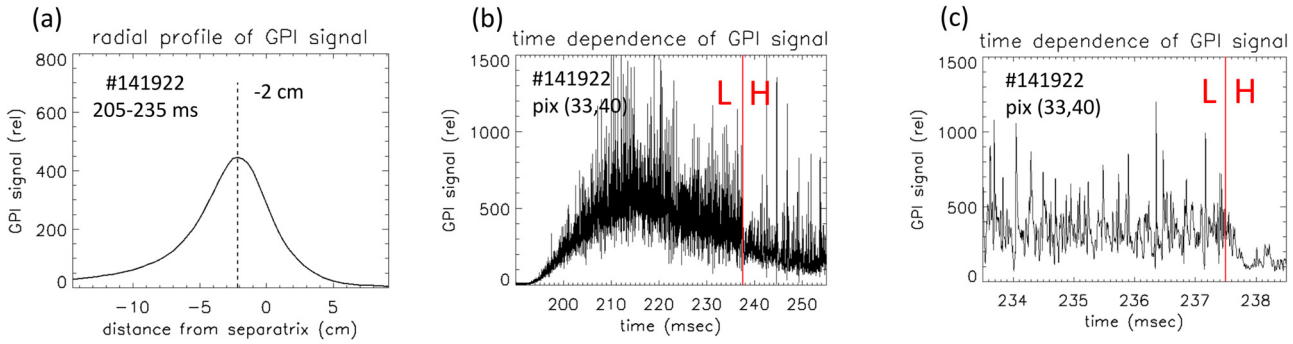

FIG. 7. Examples of GPI signals for shot #141922. In (a) is the radial profile of the signal amplitude before the L-H transition showing the signal level peaking at –2 cm inside the separatrix. In (b) is the time dependence of the GPI signal at a single pixel, and in (c) is the same signal on a faster timescale near the transition (red line). The relative fluctuation level decreases significantly at the transition, at least before the ELMs start.

been detected by Mirnov coils in NSTX. The maximum spectral power of these poloidal velocity oscillations in the L-mode occurs ~8 ms before the L-H transition, as indicated by the vertical white line labeled "max." During the 10 ms after the transition the oscillating zonal flow is absent, but it reappears after the H-L transition at 265 ms.

Figure 4(b) shows the radial profile of the $\langle V_{pol}\rangle_{pol}$ power spectrum at the time of its maximum in Fig. 4(a), i.e., at 246 ms, which is ~8 ms before the transition. The frequency of the zonal flow spectrum at this time is ~3 kHz over the radial range of –4 to 0 cm inside the separatrix. The radial profiles of the spectrum at other times are also nearly flat, which is consistent with the similarity of these $\langle V_{pol}\rangle_{pol}$ at different radii in Fig. 3(b). The magnitude of the 3 kHz oscillation diminishes rapidly outside the separatrix at $r = 0$ cm, even though the GPI signal level is still fairly high there, as seen in Fig. 2(a). These results show that the zonal flows before the L-H transition are correlated over a radial width of ~4 cm just inside the separatrix. Typical radial profiles of $\langle V_{pol}\rangle_{pol}$ for this shot are shown in Fig. 12(a).

An important issue for this paper is whether changes in the turbulence poloidal velocity trigger the L-H transition. To help answer this question, Fig. 5 shows the fluctuation level in $\langle V_{pol}\rangle_{pol}$ vs time at three radii just inside the separatrix. This is calculated as the standard deviation of the $\langle V_{pol}\rangle_{pol}$ shown in Fig. 3, where a 1 ms time average was taken before each time point. The estimated uncertainty in $\langle V_{pol}\rangle_{pol}$ due to small-scale turbulence motion is ±0.5 km/s, as discussed in the Appendix. There is no clear and consistent increase in the $\langle V_{pol}\rangle_{pol}$ fluctuation level during the last few milliseconds before the transition.

Another important issue is the relationship between $\langle V_{pol}\rangle_{pol}$ and the local density fluctuations, which may determine the effects of $\langle V_{pol}\rangle_{pol}$ on edge plasma transport. Previous results on NSTX[9] showed that the GPI fluctuation levels could be strongly correlated with 3–4 kHz oscillations in $\langle V_{pol}\rangle_{pol}$ similar to those shown in Fig. 4(a). Although very interesting, a detailed analysis of this relationship is beyond the scope of this paper (as defined by its title).

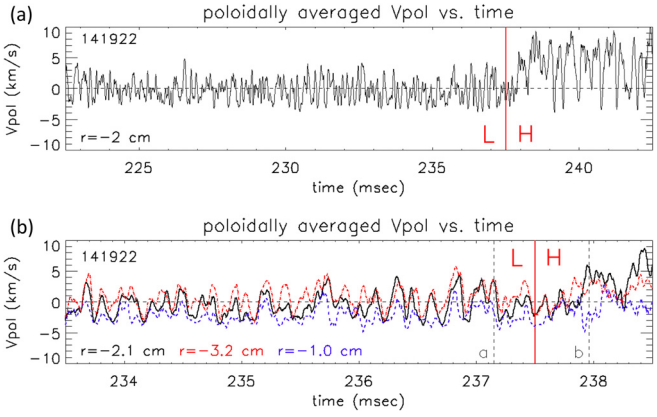

FIG. 8. Poloidally averaged poloidal velocity analysis for shot #141922. Part (a) shows $\langle V_{pol}\rangle_{pol}$ at a radius of –2 cm inside the separatrix from 15 ms before to 5 ms after the L-H transition (red line). These $\langle V_{pol}\rangle_{pol}$ do not show near-periodic oscillations as they did in Fig. 3. The same $\langle V_{pol}\rangle_{pol}$ signal is shown in black in part (b) over 5 ms near the L-H transition, and overlaid with $\langle V_{pol}\rangle_{pol}$ results from radii of –3 cm and –1 cm. The times of the images in Fig. 1 are shown in as the vertical dashed lines (a) and (b). A positive $\langle V_{pol}\rangle_{pol}$ is in the electron diamagnetic direction.

B. Second example: #141922

We now discuss a second example of the GPI signals and poloidally averaged poloidal velocities near the L-H transition. This is for a shot #141922 in which the L-H transition occurs about 30 ms after the start of a 0.7 MW RF heating pulse (see Table I).

The top two rows of Fig. 6(a) show 12 successive frames covering 30 μs of GPI image data taken at about 0.4 ms before the L-H transition shot #141922. These frames were chosen to illustrate the complex turbulence structure and motion in this shot, which does *not* show clear poloidal velocity oscillations as did Fig. 1. The turbulence in this second shot changes shape and velocity significantly within this 30 μs, and has significant outward blob propagation as well. This complex structure and motion can best be appreciated by viewing the videos in the supplementary material or in.[31]

The third row of frames in Fig. 6(b) was taken about 0.4 ms after the L-H transition and shows a narrow radial GPI profile with relatively little turbulence structure or motion, indicating a quiescent H-mode state, similar to Fig. 1(c). However, in this shot some fluctuations are still visible after the transition, such as the upward propagation of the brightest region in Fig. 6(b).

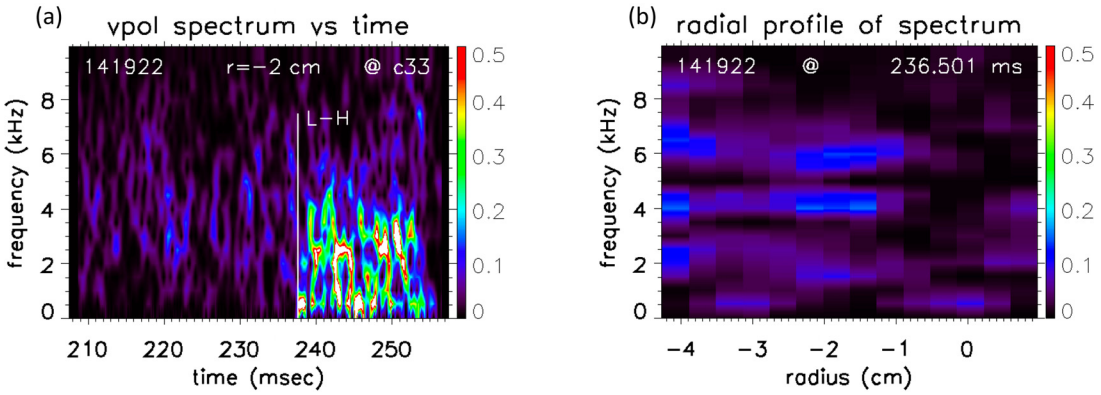

FIG. 9. Power spectra of the $\langle V_{pol}\rangle_{pol}$ fluctuations at –2 cm for shot #141922, plotted similarly to those in Fig. 3(a) for #138113. For #141922 there is no single coherent zonal flow oscillation before the L-H transition as there was for #138113, and the magnitude of the power spectral fluctuations preceding the transition is much lower. Part (b) shows the radial profile of the power spectra of $\langle V_{pol}\rangle_{pol}$ at 1–2 ms before the L-H transition in this shot. There are several frequency components, showing a more complex velocity fluctuation spectrum than for shot # (138113).

Figure 7(a) shows the radial profile of the GPI signal averaged over 30 ms during the L-mode time period before the transition, where the horizontal coordinate is the distance from the local separatrix at row #40, and the vertical scale is the average GPI signal over rows 10–69. As in the first example in Fig. 2, the GPI signal peaks about –2 cm inside the separatrix, but here the separatrix was located nearer to the outer limiter for better RF coupling. Figure 7(b) shows the time dependence of the raw GPI signal at a single pixel radially nearest to –2 cm (column #33) and poloidally at the vertical center of the image (row #40), after smoothing over ±1 pixel. The relative GPI signal fluctuation level decreases significantly at the L-H transition time of 237.5 ms (red line), but then goes back up starting about 5 ms later, mainly due to ELMs with a period of 2–3 ms. Figure 7(c) shows the transition time in more detail. This relative fluctuation level decreases significantly during the first 1 ms after the transition (before the ELMs start), when the radial profile of the GPI signal narrows due to profile changes, as shown in Fig. 6(c).

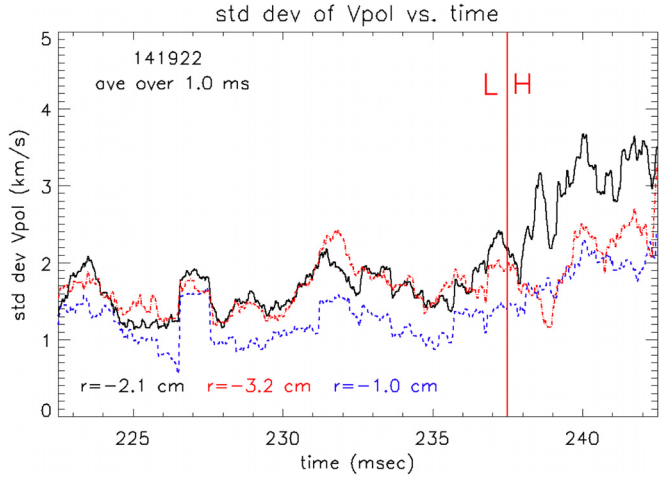

FIG. 10. The fluctuation level (standard deviation) of the $\langle V_{pol}\rangle_{pol}$ velocity vs time at three radii just inside the separatrix for shot #141911. The time-average is taken over 1 ms preceeding each time point. The $\langle V_{pol}\rangle_{pol}$ fluctuation level is not consistently large during the last 1 ms, before the transition, compared with the 10 ms period before the L-H transition.

Figure 8 shows the poloidal velocity analysis for shot #141922, as done in Fig. 3 for shot #138113. Figure 8(a) shows the poloidally averaged turbulence velocity $\langle V_{pol}\rangle_{pol}$ at a radius of –2 cm inside the separatrix for a time period from 15 ms before to 5 ms after the L-H transition at 237.5 ms (red line). The calculated $\langle V_{pol}\rangle_{pol}$ do *not* have a single near-periodic oscillation as they did in Fig. 3, and the calculated $\langle V_{pol}\rangle_{pol}$ is not significantly changing in the few milliseconds just before the transition. The poloidal velocity after the transition becomes significantly more positive (i.e., in the electron diamagnetic direction), and has a higher fluctuation level.

The same $\langle V_{pol}\rangle_{pol}$ is shown in black in Fig. 8(b) from 4 ms before to 1 ms after the L-H transition, and overlaid with $\langle V_{pol}\rangle_{pol}$ signals from radii of –3 and –1 cm (i.e., columns #28 and 36), as shown in red and blue. These $\langle V_{pol}\rangle_{pol}$ signals are similar to each other, but not as similar to those in the first example of Fig. 3(b), and none show any significant $\langle V_{pol}\rangle_{pol}$ changes in the few milliseconds before the L-H transition. The times of the GPI images of Fig. 6 are shown in Fig. 8(b) as vertical dashed lines labeled (a) and (b).

Figure 9(a) shows the power spectrum of the $\langle V_{pol}\rangle_{pol}$ flows at –2 cm for shot #141922, as done in Fig. 4(a) for #138113. For #141922 there is no single coherent zonal flow oscillation preceding the L-H transition, and the magnitude of the power spectral fluctuations is significantly lower than #138113 (with the same color scale). The power spectral fluctuations of $\langle V_{pol}\rangle_{pol}$ at this radius increase after the transition, partly due to residual turbulence and partly to ELMs. Figure 9(b) shows the radial profile of the power spectra of $\langle V_{pol}\rangle_{pol}$ at 1 ms before the L-H transition, which includes the time of the images in Fig. 6(b). There are several frequency components visible, showing a more complex velocity fluctuation spectrum than shot #138113.

Typical radial profiles of $\langle V_{pol}\rangle_{pol}$ for this shot are shown in Fig. 12(b).

Figure 10 shows fluctuation levels (standard deviations) in $\langle V_{pol}\rangle_{pol}$ for shot #141922 at three radii inside the separatrix. As for Fig. 5, the time average for this calculation is taken over the 1 ms

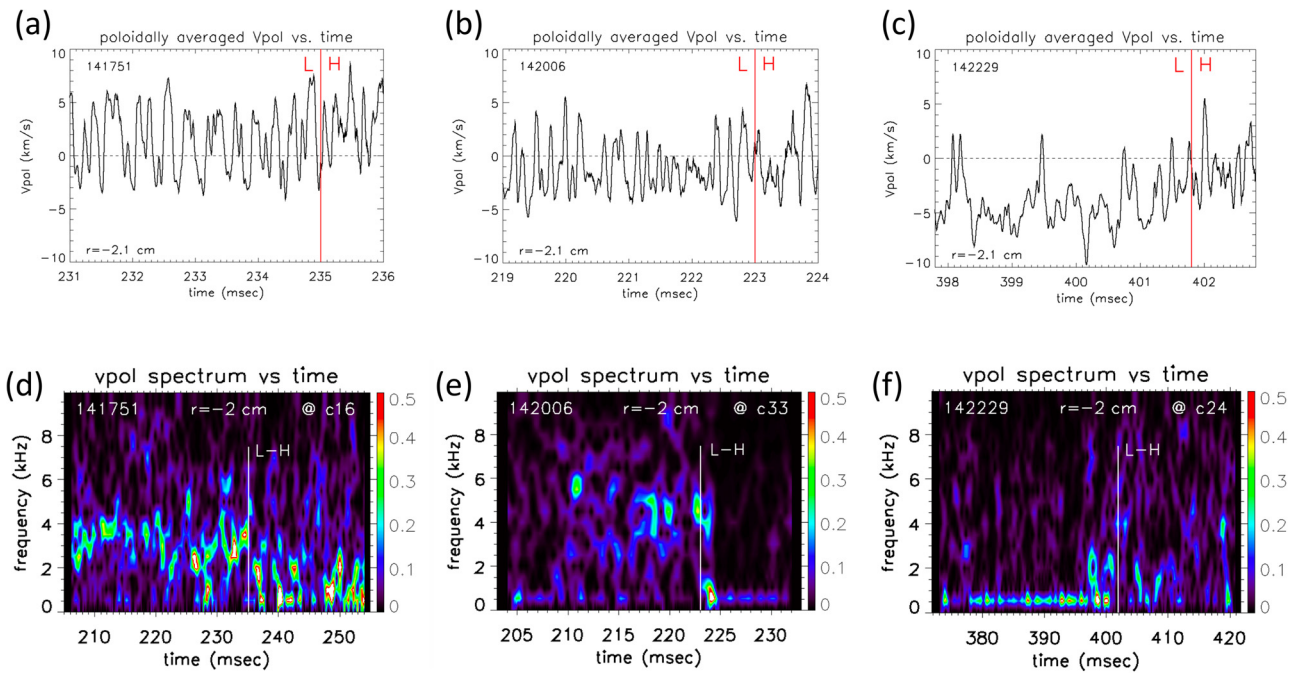

FIG. 11. Three other examples of poloidal flow analysis from Table I; namely for #141751 (Ohmic), #142006 (RF) and #142229 (NBI). Poloidally averaged poloidal velocities vs time for these shots at –2 cm inside the separatrix are shown on a 5 ms timescale in (a)–(c), similarly to Figs. 3(b) and 8(b). Power spectra of $\langle V_{pol} \rangle_{pol}$ vs time and frequency at this radius are shown over longer timescales in (d)–(f), using the same color scale as in Figs. 4(a) and 9(a).

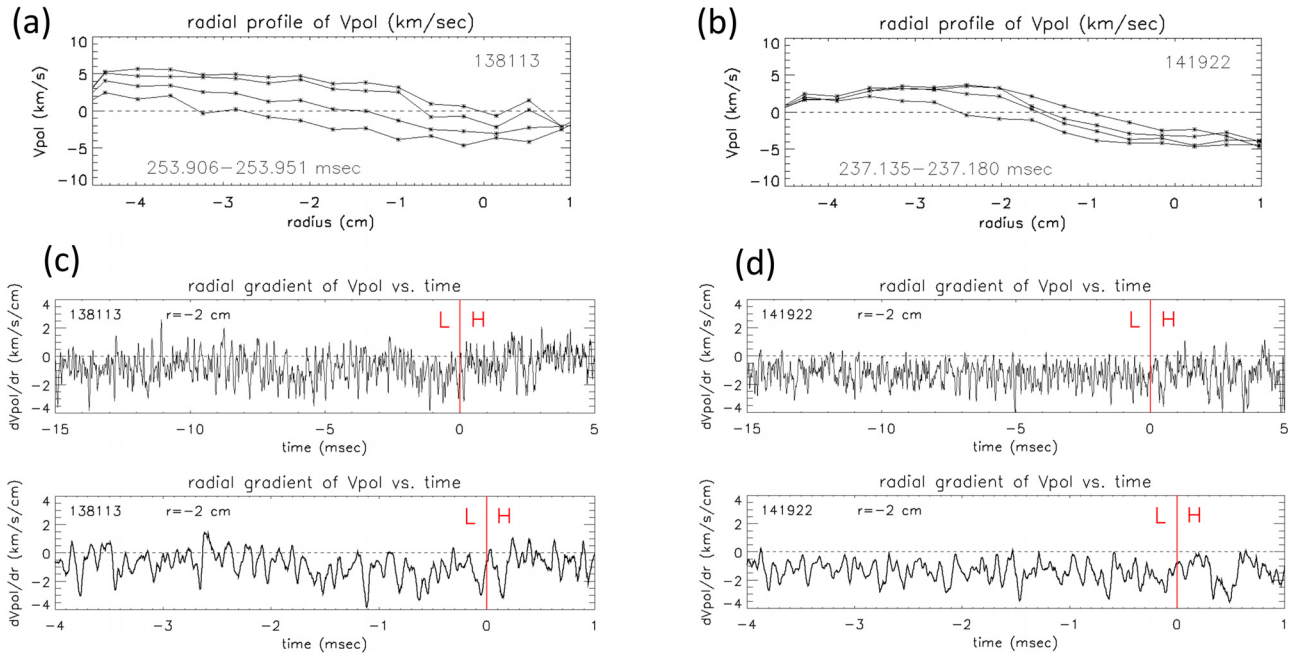

FIG. 12. Parts (a) and (b) show typical radial profiles of $\langle V_{pol} \rangle_{pol}$ for shots #138113 and #141922, respectively. Parts (c) and (d) parts show the radial turbulence velocity gradient of $\langle V_{pol} \rangle_{pol}$ vs the time with respect to the L-H transition (red lines) evaluated at a radius of –2 cm inside the separatrix for shots #138113 and #141922, respectively. The top parts of (c) and (d) shows the results from –15 ms before to 5 ms after the L-H transition, and the bottom parts show the results for a shorter timescale from –4 ms before to 1 ms after the transition.

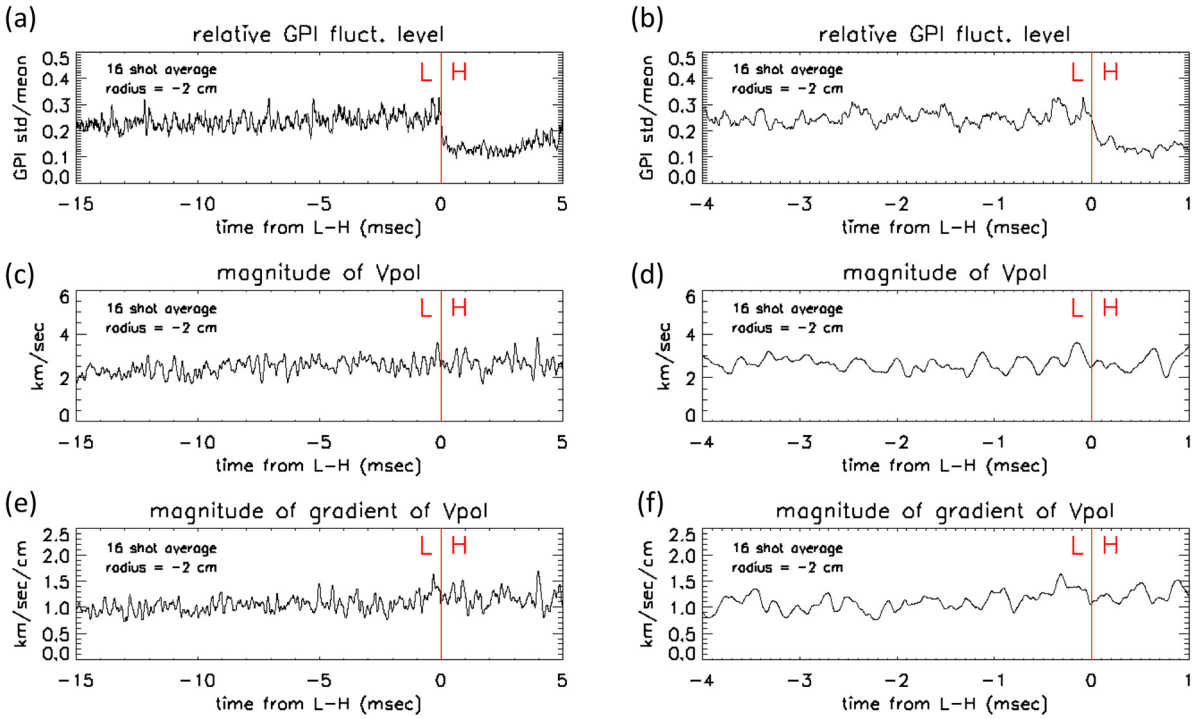

FIG. 13. Shot-averaged quantities vs time at a radius of –2 cm for the entire 16 shot database. The time range from 15 ms before to 5 ms after the L-H transition at the left, and the timescale from 4 ms before to 1 ms after the transition is at the right. Parts (a) and (b) show the relative GPI fluctuation level, which decreases significantly at the L-H transition. Parts (c) and (d) show the shot-averaged magnitude of $|V_{pol}|$, and parts (e) and (f) show the shot-averaged magnitude of the radial gradient $|\text{grad } V_{pol}|$.

preceding each time point. In the 10 ms before the transition the average fluctuation levels are roughly half those of shot #138113. Although the fluctuation level at –2 cm inside the separatrix is slightly higher in the last 1 ms before transition, it is not higher for the other two radii. The estimated uncertainty in $\langle V_{pol}\rangle_{pol}$ due to small-scale turbulence motion is ±0.5 km/s, so the $\langle V_{pol}\rangle_{pol}$ fluctuation level is not changing significantly before the transition.

C. Other examples

Figure 11 shows three other examples of poloidal velocity analysis of shots from Table I; namely #141751 (Ohmic), #142006 (RF), and #142229 (NBI). Poloidally averaged poloidal velocities vs time for these shots at radii of –2 cm inside the separatrix are shown on a 5 ms timescale in Figs. 11(a)–11(c), similarly to Figs. 3(b) and 8(b). Power spectra of $\langle V_{pol}\rangle_{pol}$ vs time and frequency at this radius are shown over longer timescales in Figs. 11(d)–11(f), using the same color scale as in Figs. 4(a) and 9(a).

The $\langle V_{pol}\rangle_{pol}$ signals and spectra for the Ohmic shot #141751 in Figs. 11(a) and 11(d) look qualitatively similar to the first example. The velocity fluctuation level does not change significantly in the 4 ms before the transition, and the power spectrum has a near-coherent but intermittent peak near 3–4 kHz during the 30 ms before the L-H transition. The $\langle V_{pol}\rangle_{pol}$ signals for the RF shot #142006 in Fig. 11(b) are more irregular vs time, but the spectra in Fig. 11(e) have a few small peaks near 5 kHz during the 10 ms before the transition. The $\langle V_{pol}\rangle_{pol}$ signals for the NBI shot #142229 in Fig. 11(c) are even more irregular vs time in the 4 ms before the transition, and the power spectra of #142229 in Fig. 11(f) show mainly 0.5 kHz bursts for about 30 ms before the L-H transition. Therefore, the $\langle V_{pol}\rangle_{pol}$ signals and spectra show considerable shot-to-shot variability, as did the first two examples.

Power spectra were made of the $\langle V_{pol}\rangle_{pol}$ at –2 cm inside the separatrix for all 16 shots of Table I during the ∼30 ms preceding the L-H transition. Seven shots had a nearly coherent spectral feature in the range ∼2–5 kHz (138113, 138116, 138118, 138119, 141746, 141747, 141751), similar to that in Fig. 4(a). For all seven shots the frequency of this zonal flow feature was nearly constant over ∼0–4 cm inside the separatrix, as shown in Fig. 4(b), including both Ohmic and NBI heated shots. This appears to contrast with TJ-II results [26] in which the radial width of the zonal flow was different in NBI and electron cyclotron heated plasmas. None of these seven shots had a significant increase in the magnitude of the coherent velocity oscillation magnitude just before the transition. Four other shots (138114,138115,138117,142006) had a slightly coherent zonal flow feature similar to Fig. 11(e). Three shots #141919–141922 had no clear velocity spectrum peak, as in Fig. 9(a), and two shots #139955 and 142229 with NBI showed a bursting feature at ∼0.5 kHz, as in Fig. 11(f), but without any significant velocity changes just before the transition.

Although the goal of this paper is to analyze the turbulence velocities preceding the L-H transition, we add here some comments on the $\langle V_{pol}\rangle_{pol}$ in H-mode after the transition at –2 cm inside the separatrix. For the first example of Fig. 3 (#138113), the time-averaged value of

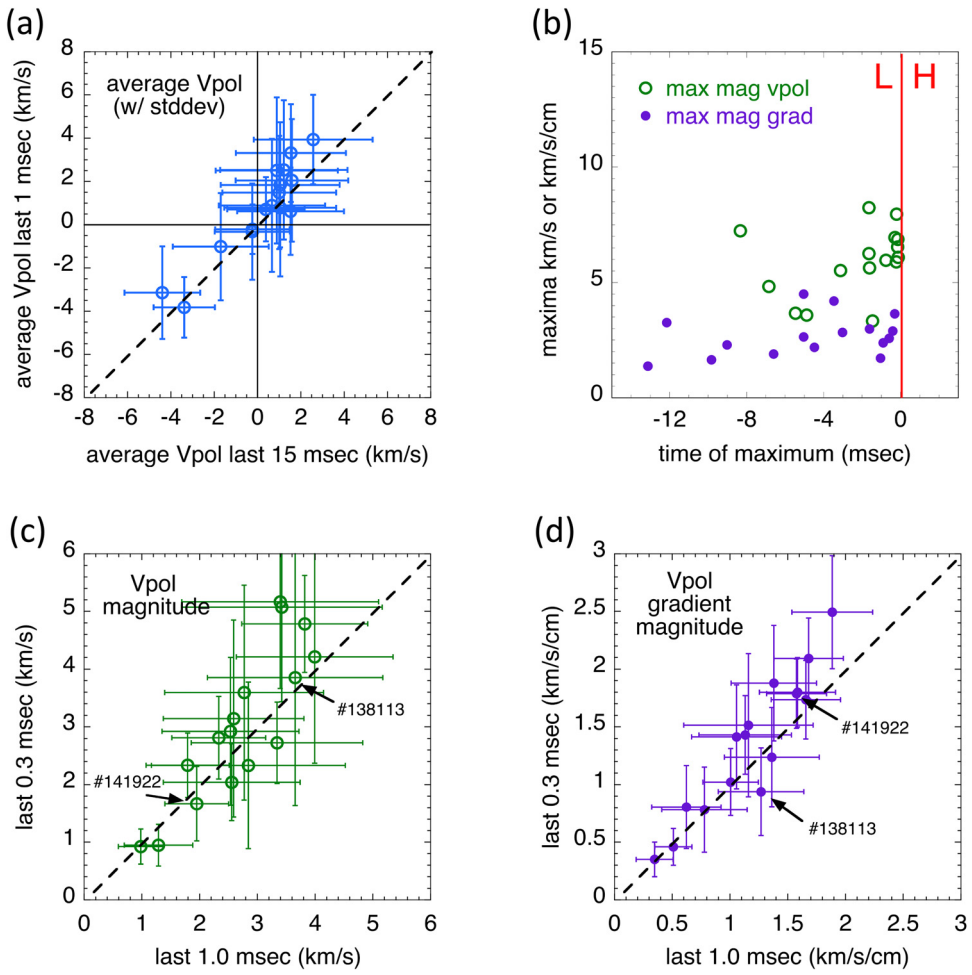

FIG. 14. Part (a) shows the average values of $\langle V_{pol}\rangle_{pol}$ over the last 1 ms before the L-H transition vs its average values over the last 15 ms for all 16 shots in the database. Part (b) shows the maximum value of $|V_{pol}|$ and $|\text{grad } V_{pol}|$ vs their timing with respect to the L-H transition. Parts (c) and (d) compare time averages of these two quantities over the last 0.3 ms before the transition (vertical) to averages over the last 1.0 ms before the transition (horizontal). The standard deviations of $\langle V_{pol}\rangle_{pol}$ and $|V_{pol}|$ are shown as error bars in (a) and (c), and the uncertainties in the velocity gradient fits are shown as error bars in (d).

$\langle V_{pol}\rangle_{pol}$ *decreased* from +2.5 km/s for the period between −1.1 to −0.1 ms before the transition to +0.6 km/s for the period between +2.0 and 3.0 ms after the transition. However, for the second example of Fig. 8 (#141922), the time-averaged value of $\langle V_{pol}\rangle_{pol}$ *increased* significantly from −0.3 km/s for the period between −1.1 and −0.1 ms before the transition to +4.5 km/s for the period between +2.0 and 3.0 ms after the transition. For the three other examples used in Fig. 11, the corresponding velocity changes at these same times were: (a) for 141751, from +1.8 km/s before to +4.1 km/s after the transition, (b) for 142006, from −1.0 km/s before to −3.4 km/s after the transition, and (c) for 142229, from −3.1 km/s before to −2.0 km/s after the transition (note that the times from +2 to 3 ms are not shown in Fig. 11). In the 16 shot database, the values of $\langle V_{pol}\rangle_{pol}$ at these same times increased from before to after the transition by more than +2 km/s in 5 shots, decreased by more than −2 km/s in 4 shots, and changed by less than 2 km/s in 7 shots. The largest increase in velocity between these times was +4.8 km/s (#141922), and the largest decrease was −5.6 km/s (#141746), but the shot-averaged change was nearly zero to within ±1 km/s. This widely varying behavior is discussed further in Sec. IV C.

D. Turbulence velocity shear

The radial gradient of the poloidal turbulence velocity, or turbulence velocity shear, is relevant for the L-H transition, since an increase in this gradient can change the structure and transport effects of the turbulence.[2] The local poloidal velocity shear of the turbulence itself can be estimated from the poloidally averaged poloidal velocities $\langle V_{pol}\rangle_{pol}$ obtained from the GPIFLOW code for this GPI data (see the Appendix). Note that this velocimetry analysis does *not* attempt to identify any individual blob-like structures in the image data, but instead uses the normalized time-delayed cross correlation functions of the unfiltered time series of GPI image pixels. Thus, the gradients discussed in this section involve only these turbulence velocity

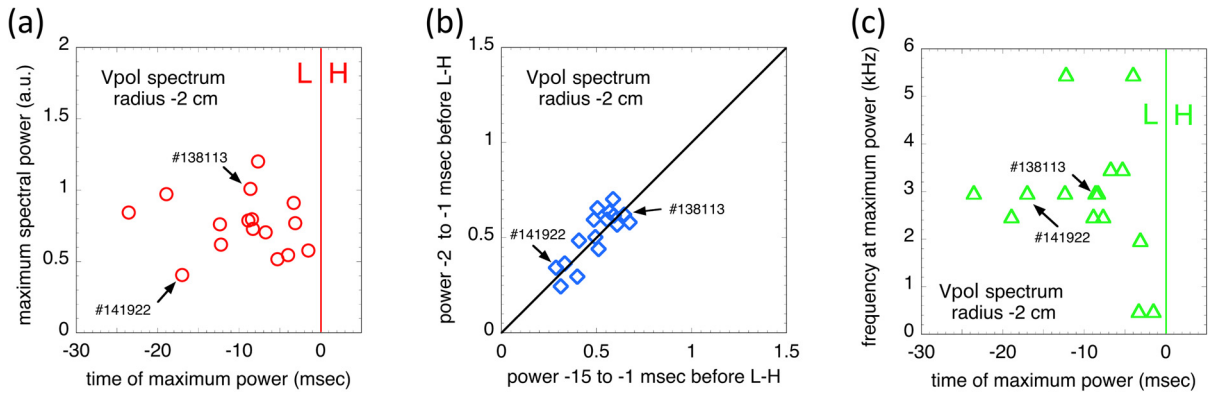

FIG. 15. Part (a) shows the magnitude of the peak $\langle V_{pol}\rangle_{pol}$ spectral power (in arbitrary units) as a function of the timing of this peak with respect to the L-H transition. Part (b) shows the time average of the peak spectral power of $\langle V_{pol}\rangle_{pol}$ at 1–2 ms before the transition (horizontal) vs the time-average of the peak spectral power over the last 15 ms before the transition (vertical). Part (c) shows the frequency at the peak $\langle V_{pol}\rangle_{pol}$ spectral power as a function of its time with respect to the transition.

gradients measurable by the GPI diagnostic, which are not necessarily the same as the shear in the radial electric field or shear in the poloidal fluid flow, as discussed further in Sec. IV C.

Figures 12(a) and 12(b) show typical radial profiles of $\langle V_{pol}\rangle_{pol}$ for shots #138113 and #141922, respectively. These sample profiles are shown for four successive frames separated by 15 μs during the time periods just before the L-H transition used in Figs. 1(a), 1(b), and 6(a). Each radial point corresponds to one column in the GPI image. These and other $\langle V_{pol}\rangle_{pol}$ radial profiles are fairly smooth and vary slowly from frame-to-frame, which allows the radial turbulence velocity gradient to be evaluated on a 2.5 μs timescale before the transition.

Figures 12(c) and 12(d) show the radial gradient of $\langle V_{pol}\rangle_{pol}$ vs time as evaluated at a radius of –2 cm inside the separatrix by making a linear fit of the $\langle V_{pol}\rangle_{pol}$ over a radial distance of ±1.1 cm, i.e., over ±3 columns (i.e., 7 radial points) around the column nearest –2 cm. This was done at each time point in the GPI data, i.e., with a time resolution of 2.5 μs. The results for the first example #138113 are shown in Fig. 12(c), and for the second example #141922 in Fig. 12(d). The top figure in both parts shows the results from –15 ms before to 5 ms after the L-H transition, and the bottom figure shows the results for a shorter timescale from –4 ms before to 1 ms after the transition.

The radial gradient of $\langle V_{pol}\rangle_{pol}$ vs time for shot #138113 in Fig. 12(c) fluctuates over a range from –4 to +2 km/s cm, where the negative sign implies the velocity is increasingly negative with increasing radius. The time-averaged radial gradient for #138113 during the 15 ms before the L-H transition is –0.8 ± 0.9 km/s cm, with no significant trend vs time and no unusual variation within 4 ms before the transition. The time-averaged radial gradient for shot #141922 in Fig. 12(d) during the 15 ms before the L-H transition is –1.3 ± 0.7 km/s cm, with a slight trend toward increasingly negative gradient with time, but again with no unusual variation during the 4 ms before the transition. The uncertainty (standard deviation) in the linear fits at each frame used to find these radial gradients were ±0.34 and ±0.29 km/s cm, averaged over the 15 ms preceding the transition for #138113 and #141922, respectively.

The radial gradients of $\langle V_{pol}\rangle_{pol}$ vs time at a radius of –2 cm for the other three shots of Fig. 11, averaged over the 15 ms preceding the L-H transitions, were –1.5 ± 1.0 km/s cm for #141751, –1.0 ± 0.7 km/s cm for #142006, and –0.03 ± 0.4 km/s cm for #142229 (i.e., near zero). The uncertainty (standard deviation) in the ±3 column linear fits at each frame used to find these gradients were ±0.28, ±0.26, and ±0.13 km/s cm, respectively, averaged over the 15 ms preceding the transition. There were no clear increases in these radial turbulence velocity gradients during the 4 ms preceding the L-H transition.

Although the focus of this paper is on the turbulence velocity preceding the L-H transition, it is interesting to note that there does not appear to be a significant change in the radial velocity gradients vs time from L-mode to H-mode in the two shots of Figs. 12(c) and 12(d). This is discussed further in Sec. IV C.

E. Velocity database

This section describes the poloidal velocity variations over the 16 shot database of Table I, including both the shot-averaged velocities and their shot-to-shot variations. Since the poloidal turbulence velocities $\langle V_{pol}\rangle_{pol}$ can be much larger than their time averages, as shown in Figs. 3 and 8 and previously,[10] we mainly use the absolute values $\langle V_{pol}\rangle_{pol}$ at each time frame to characterize the magnitude of the poloidally averaged poloidal velocities, which we abbreviate as $|V_{pol}|$. The radial gradients of poloidal turbulence velocity were calculated using linear fits to $\langle V_{pol}\rangle_{pol}$, as described in Sec. III D, and the absolute magnitude of these radial gradients |grad V_{pol}| was used in the velocity database, since the radial gradients can be of either sign (as shown in Fig. 12).

Even though these 16 shots have different heating power and edge parameters, we first check whether there are any consistent trends in the shot-averaged time dependences preceding the L-H transition. Figure 13 shows shot-averaged results at a radius of –2 cm inside the separatrix, where the plots on the left show the time period from 15 ms before to 5 ms after the L-H transition, and the plots on the right side show the period from 4 ms before to 1 ms after the transition. The values for each shot were averaged over 0.1 ms (40 frames), and the transition times are shown by the red vertical lines. In Figs. 13(a) and 13(b) is the relative GPI signal fluctuation level evaluated at a single pixel (smoothed over ±1 pixel) at the image column nearest to –2 cm, and poloidally at the vertical center of the image (as in Figs. 2 and 7). In Figs. 13(c) and 13(d) is the magnitude of the

poloidal velocity $|V_{pol}|$, and in Figs. 13(e) and 13(f) is the magnitude of the radial gradient of the poloidal velocity |grad V_{pol}|.

The shot-averaged GPI fluctuation level in Figs. 13(a) and 13(b) falls rapidly and significantly across the transition; namely, from 25% ± 3% during the 1 ms period from −1.1 to −0.1 ms before the transition to 13 ± 1% during the 1 ms period from 0.2 to 1.2 ms after the transition. Note that since the timing of the L-H transition is uncertain by about ±0.1 ms, this period around the transition time was not used for these averages. The rapid decrease in fluctuation level at the transition is similar to that shown previously at −1 cm inside the separatrix.[10]

The velocity and velocity gradients in Fig. 13 are varying due to the time evolution of the auxiliary heating and plasma conditions in these relatively short discharges. The shot-averaged magnitude of the poloidal velocity $|V_{pol}|$ in Figs. 13(c) shows a slow increase over this time from 2.2 ± 0.2 km/s during 15–14 ms before the transition to 2.7 ± 0.4 km/s from −1.1 to 0.1 ms before the transition. The shot-averaged magnitude of the gradient of the poloidal velocity also increases from 0.94 ± 0.08 km/s to 1.3 ± 0.2 km/s cm over this time. It is potentially interesting that the shot-averaged velocity and velocity gradient in Fig. 13 are both largest within the last 1 ms before the transition. However, the shot-to-shot variations are considerably larger than these relatively small variations over time, as described next. Also, the turbulence velocity and velocity gradients in Fig. 13 do not appear to change from just before to just after the L-H transition, as discussed further in Sec. IV C.

Figure 14 shows poloidal velocity results from the 16 individual shots in the database. To start, Fig. 14(a) shows the time-averaged poloidal velocity $\langle V_{pol}\rangle_{pol}$ (such as shown in Figs. 3 and 8) from −1.1 to −0.1 ms before the L-H transition (vertical axis) vs its average value during the last 15 ms before the transition (horizontal), where the error bars show the standard deviations in these signals over these times. The time period within 0.1 ms of the transition was not included since the transition time is uncertain to within ±0.1 ms. These two time averages in Fig. 14(a) are nearly the same for all shots (within a standard deviation), showing that the average poloidal velocities are not changing significantly in the last 1 ms before the transition. More interesting is the wide range in these poloidal velocities, e.g., from about −4 km/s in the ion diamagnetic direction for the shots #139955 and #142229 (with long duration NBI) to +4 km/s for in the electron diamagnetic direction for shot #138119 (with short duration NBI). It is possible that the large negative velocities are due in part to beam-induced toroidal rotation, but direct toroidal rotation measurements are not available for these shots.

Figure 14(b) shows the times of the maximum value of the magnitude of $|V_{pol}|$ and the magnitude of its radial gradient |grad V_{pol}| at a radius of −2 cm during the 15 ms preceding the L-H transition. The maximum values of $|V_{pol}|$ occurred within the final 1 ms before the transition in 7/16 shots, and the maximum values of |grad V_{pol}| occurred within the final 1 ms before the transition in only 4/16 shots. The maxima in $|V_{pol}|$ occurred up to 8.3 ms before the transition, and the maxima in |grad V_{pol}| occurred up to 13.1 ms before the transition. This broad distribution in timing implies that these maxima did not consistently trigger the L-H transition in these shots.

To further clarify the poloidal velocities changes just before the transition, Figs. 14(c) and 14(d) show the time-averaged values of $|V_{pol}|$ and |grad V_{pol}| in the last 0.3 ms before the transition (i.e., −0.4 to −0.1 ms) vs their time-averaged values over the last 1.0 ms (i.e., −1.1 to −0.1 ms). The standard deviations of the $|V_{pol}|$ are shown as error bars in Fig. 14(c), and the time-averaged uncertainty in the linear gradient fits for each shot are shown by the error bars in Fig. 14(d). For almost all shots, the differences between these two times were not significant, i.e., less than the error bars. Although the shot-averaged velocity gradient in Fig. 14(d) was 0.17 km/s cm larger for the last 0.3 ms than for the last 1.0 ms (i.e., most points were above the dashed line), this difference is less than the shot-averaged uncertainty in the velocity gradient in the last 0.3 ms of 0.25 km/s cm. Note that the shots with the lowest velocity gradient were #139955 and #142229, which were the shots with the largest negative velocity in the ion diamagnetic drift direction of Fig. 14(a).

The dominant result from Figs. 14(c)–14(d) is the significant variability in the values of $|V_{pol}|$ and |grad V_{pol}| among these 16 individual shots. For example, in the last 1 ms before the transition $|V_{pol}|$ ranged from 1.0 to 4.0 km/s, and |grad V_{pol}| ranged from 0.34 to 1.9 km/s cm. These shot-to-shot variations are considerably larger than the time variations in the shot-averaged values shown in Fig. 13, in which $|V_{pol}|$ increased by 0.5 km/s and |grad V_{pol}| increased by 0.35 km/s cm during the period from 15 to 1 ms before the transition. The values of $|V_{pol}|$ and |grad V_{pol}| during −1.1 to −0.1 ms at a radius of −2 cm for each shot are listed in Table I. There is only a small cross correlation coefficient of −0.2 between $|V_{pol}|$ and |grad V_{pol}| for these 16 shots, suggesting that there is no simple relationship between these two quantities.

Among groups of shots with different types of heating in Table I, the NBI shots have the highest velocities with $|V_{pol}| = 3.3 \pm 0.9$ km/s, the RF shots have the lowest velocities at $|V_{pol}| = 1.6 \pm 0.6$ km/s, and the Ohmic are in between at $|V_{pol}| = 2.9 \pm 0.4$ km/s. As noted in Sec. II B, the time of the auxiliary heating with respect to the L-H transition also varied; namely, three shots had the L-H transitions occurring ≤20 ms of the start of NBI heating (#138113, 138114, 138119), two shots had the transitions occurring ≥100 ms after the start of NBI (#139955, 142229), and the four shots had the transitions occurring ∼20–40 ms after the start of RF heating. Therefore, among the shots with auxiliary heating there is likely to be a varying edge toroidal velocity at the transition which may be affecting these $|V_{pol}|$, which is a hidden variable since it was not directly measured in these experiments. Note that the shots with Ohmic heating have fairly self-consistent $|V_{pol}|$, for example, the 4 shots #138115–138118 had $|V_{pol}| = 2.9 \pm 0.4$ km/s.

The seven shots with the clearest zonal flow oscillations such as Fig. 4(a) (as listed in Sec. III C) have averages of $|V_{pol}| = 3.1 \pm 0.6$ km/s and |grad V_{pol}| = 1.4 ± 0.4 km/cm s, while the other nine shots have averages of $|V_{pol}| = 2.4 \pm 1.0$ km/s and |grad V_{pol}| = 1.0 ± 0.5 km/cm s, both of which are marginally lower. The three shots with smallest zonal flow oscillations such as Fig. 9(a) have $|V_{pol}| = 1.4 \pm 0.5$ km/s and |grad V_{pol}| = 1.4 ± 0.3 km/cm s, suggesting a trend for $|V_{pol}|$ to decrease with lower zonal flow oscillations, as also shown in Fig. 14(b).

It is not yet clear what causes these shot-to-shot variations of $|V_{pol}|$ and |grad V_{pol}|. This is not too surprising since previously measured variations in edge turbulence scale lengths and fluctuation levels in NSTX are not yet well understood either,[28] mainly because nonlinear edge turbulence simulations are still under development. The present database of 16 L-H transitions is a representative sampling from

NSTX, but is not a large enough data set to infer statistically meaningful empirical scalings of the poloidal velocity.

F. Velocity spectrum database

The power spectra vs frequency of the poloidally averaged $\langle V_{pol}\rangle_{pol}$ at −2 cm inside the separatrix were previously shown for two sample shots in Figs. 4(a) and 9(a). The first of these shots (#138113) showed a near-periodic oscillation in the spectrum for about 20 ms before the L-H transition, but the second shot (#141922) did not. This section presents a database characterizing the peak levels of these power spectra, which provides a measure of how well these velocity oscillations are correlated with the L-H transition in all 16 shots. These $\langle V_{pol}\rangle_{pol}$ power spectra were calculated at −2 cm inside the separatrix for up to 30 ms before the L-H transition using a moving time interval of ± 1 ms (±400 frames), with a frequency resolution of 0.5 kHz up to 20 kHz. The peak level of the spectral power vs time was found with a timing accuracy of 0.625 ms (with a ±1 ms width of the Fourier analysis).

Figure 15(a) shows the magnitude of the peak levels of the $\langle V_{pol}\rangle_{pol}$ spectral power (in arbitrary units) as a function of its timing with respect to the L-H transition (only peaks at times more than 1 ms before the transition were used to avoid overlapping the H-mode phase). These peaks occurred more than 4 ms before the transition in 12 shots, and between 4 and 1 ms before the transition for only 4 shots. Thus for most shots the peak in the $\langle V_{pol}\rangle_{pol}$ spectrum occurred well before the L-H transition.

Figure 15(b) shows the time average of the peak spectral power from 2 to 1 ms before the transition (vertical) vs the time-average of the peak spectral power from 15 to 1 ms before the transition (horizontal). The spectral power in the last 1 ms of L-mode was not consistently larger than the spectral power over the 15 ms before the L-H transition, again showing that the spectral power of $\langle V_{pol}\rangle_{pol}$ was not unusually large just before the transition.

Figure 15(c) shows the frequency of the peak $\langle V_{pol}\rangle_{pol}$ spectral power as a function of its timing with respect to the transition. Most shots had peak frequencies in the range 2–5 kHz, but two shots with NBI had peaks at 0.5 kHz (139955,142229), such as shown in Fig. 11(c). Those shots with peaks within 10 ms before the L-H transition did not have a unique velocity spectral feature in this range.

As noted at the end of Sec. III C, only 7 of the 16 shots in this database had near-coherent zonal flow oscillations during the 15 ms preceding the L-H transition, such as shown in Fig. 4(a). Four of these seven shots had no auxiliary heating, and three of them had NBI during only part of the period of the zonal flow oscillation. Thus there is no correlation between auxiliary heating and the zonal flow oscillation, and the zonal flow oscillation is not required for an L-H transition in NSTX. The latter observation is qualitatively similar to results on other devices, as described in the Introduction.

IV. DISCUSSION

Section IV A contains a summary of the turbulence velocity results of this paper, and Sec. IV B reviews the limitations and uncertainties in these results. Section IV C discusses some interpretations of these results, and Sec. IV D gives the main conclusions.

A. Summary of turbulence velocity results

The poloidally averaged poloidal turbulence velocities $\langle V_{pol}\rangle_{pol}$ were evaluated using GPI data at −2 cm inside the separatrix where the relative fluctuation level decreased consistently at the L-H transition in NSTX. These turbulence velocities were calculated for a database of 16 shots using the analysis method described in Sec. II C and the Appendix.

Sample $\langle V_{pol}\rangle_{pol}$ results vs time were shown for five examples in Figs. 3, 8, and 11, and the magnitude of this poloidal velocity and its radial gradient was evaluated vs time for the full database in Figs. 13 and 14. In the five examples, there were no significant changes in $\langle V_{pol}\rangle_{pol}$ during 15 ms preceding the L-H transition, although the 16 shot-average poloidal velocity magnitude $|V_{pol}|$ in Fig. 13 showed a slow increase during the 15 ms before the transition. There was also no significant increase in the fluctuation level of $\langle V_{pol}\rangle_{pol}$ just before the transition, as shown in Figs. 5 and 10. The maximum values of $|V_{pol}|$ for individual shots occurred in a broad distribution up to 8 ms before the transition, as shown in Fig. 14(b), and there was a large shot-to-shot variation in the average value of $\langle V_{pol}\rangle_{pol}$ and in the magnitude of $|V_{pol}|$ during the last 1 ms before the transition, as shown in Figs. 14(a) and 14(c), respectively.

The radial gradient of $\langle V_{pol}\rangle_{pol}$ vs time was shown for two examples in Fig. 12, and the magnitude of the radial gradient |grad V_{pol}| was used for the database plots in Figs. 13 and 14. There was no clear increase in this gradient just before the transition in the two examples, although the 16 shot-averaged |grad V_{pol}| in Fig. 13 showed a slow increase during the 15 ms before the transition. The maximum values of the radial gradient for individual shots occurred in a wide distribution up to 13 ms before the transition, as shown in Fig. 14(b), and there was a large shot-to-shot variation in the magnitude of this gradient during the last 1 ms and also during the last 0.3 ms before the transition, as shown in Fig. 14(d).

The power spectrum of $\langle V_{pol}\rangle_{pol}$ was shown for five examples in Figs. 4, 9, and 11. Only two of these shots had a near-coherent zonal flow-like oscillation in the frequency range 2–5 kHz during the 15 ms preceding the L-H transition, i.e., Figs. 4(a) and 11(a). In the full database such clear poloidal velocity oscillations occurred in only 7/16 shots, while the maximum in these power spectra often occurred well before the transition, as shown in Fig. 15(a).

B. Limitations and uncertainties

A basic limitation in these results comes from the radial and poloidal range of the GPI diagnostic, which focused the radial analysis range to −2 ± 1 cm inside the separatrix and restricted the poloidal averaging range to 21 cm. Although this is several poloidal correlation lengths, the resulting $\langle V_{pol}\rangle_{pol}$ is not a true "zonal flow" averaged over the flux surface. More generally, since the turbulence velocity as measured by GPI mainly follows the apparent motion of the density perturbations (as do other optical and microwave turbulence diagnostics), this turbulence velocity cannot be used to directly measure the fluid velocity, or to separate poloidal from toroidal flows.

Another basic limitation comes from the cross correlation technique for calculating turbulence velocities, which averages over ±27.5 μs at each time point. Thus this algorithm finds only the average turbulence velocities below ∼20 kHz. The GPIFLOW code cannot accurately find the turbulence velocity when the flow reverses direction

during this averaging time (as shown in the Appendix), or during times of counter-propagating flows. The cross correlation search algorithm was limited to velocities below 15 km/s, but the resulting velocities never exceeded 10 km/s.

Another limitation was that the timing of the L-H transition as seen in the GPI fluctuation level was not defined to better than ±0.1 ms, as illustrated in Fig. 13(b). This limitation was not due to the GPI framing rate, but to shot-to-shot variations in the fluctuation level vs time over this transition period, such as shown for example, in Figs. 2(c) and 7(c).

There is uncertainty in the $\langle V_{pol}\rangle_{pol}$ due to the random motion of small-scale turbulence in the GPI images. This was estimated in the Appendix to be ±0.5 km/s based on the measured size and lifetime of the turbulence in Ohmic plasmas inside the separatrix. This approximate level of uncertainty is consistent with the coherent velocity oscillation of ∼5 km/s observed in the first example in Fig. 3, and the low-velocity fluctuation level of –0.25 ± 1.7 km/s in the second example of Fig. 8. However, there is no direct estimate of this uncertainty, since the local turbulent velocities were not directly measured and cannot be assumed consistent over time or shots.

There is also a fundamental limitation in any 2D velocimetry; namely, when the signal is exactly constant in the direction of motion, the velocity cannot be determined at all.[44] However, the motion of very small fluctuations can be detected by the cross correlation technique, since the average values in the time series are subtracted before the correlation is done. A test was made by adding to a sample of time-dependent GPI image data a constant signal 1000× larger than it, and the resulting velocity from the GPIFLOW code was exactly the same. Thus this limitation does not appear to be significant in the analysis of the $\langle V_{pol}\rangle_{pol}$ for the L-mode data in this paper, although it may be significant for quiescent periods during H-mode conditions.

C. Interpretations

This section discusses the results of this paper with respect to our evolving understanding of L-H transitions in tokamaks. In the past year alone there have been several interesting experimental results on this topic. For example, in ASDEX Upgrade, a threshold in the minimum of the poloidal ExB velocity (a proxy for the shear flow) was found to be 6.7 ± 1 km/s at the L-H transition,[45] in HL-2A, a critical value of the velocity shear at the L-H transition was found to be ∼100 kHz,[46] and in EAST the sawtooth-induced L-H transition was attributed to an increase in the edge poloidal flow shear.[47]

As mentioned in the Introduction, the GPI diagnostic does not directly measure the radial electric field or the fluid flow speed, but it does give direct information about the poloidal edge turbulence velocity. The poloidal turbulence velocity has previously been used as a proxy for the poloidal $E_r \times B$ fluid flow speed, for example, in BES[12,13] and reflectometry measurements.[16,17] However, the poloidal turbulence velocity can differ from the poloidal fluid flow due to diamagnetic flows, toroidal flows, and/or the poloidal phase velocity of waves in the rest frame of the fluid. The $E_r \times B$ velocity is perpendicular to B and hence not in the image plane of the GPI measurements, so the flow velocity along B can act as a "hidden parameter." Unfortunately, for the shots in this paper there were no measurements of the total pressure gradient or the poloidal or toroidal fluid flow profiles in the edge of NSTX, so these effects cannot be directly evaluated.

In order to fully understand the L-H transition, both the poloidal shear flow and the edge turbulence should be measured and compared with theoretical models for the shear flow stabilization. Then the effects of poloidal shear flow on the turbulence structure could be directly evaluated, and eventually the decrease in the turbulent transport at the transition can be understood. However, with the present GPI diagnostic only part of this information can be obtained, and the transport effects of the observed turbulence cannot be determined.

As mentioned in Sec. III A, the turbulence analyzed in this paper was located inside the separatrix and so cannot be identified with "blobs," which are localized in the scrape-off layer and can have additional radial motion due to the connection with the wall.[48] The large structures shown in Figs. 1(a) and 1(b) may appear to be blob-like, but are actually part of the spectrum of strong turbulence which is normally seen just inside the separatrix in NSTX and all other tokamaks. For example, the two clearest structures in both Figs. 1(a) and 1(b) move upward and downward together, as blobs do not, and the near-coherent poloidally averaged poloidal velocity oscillations seen in Fig. 3 are not a feature of blob physics. Thus the poloidal velocities determined from the turbulence analysis in this paper are not influenced by blob physics, to the best of our knowledge.

An attempt can be made to interpret the measurements in this paper with respect to the idea that the L-H transition is caused by changes in the turbulence velocity gradient. Although this theory is normally formulated in terms of the shear in the radial electric field or poloidal fluid velocity, those quantities are not measured by GPI, as described above. Instead, a dimensionless form of a turbulence decorrelation parameter can be estimated from GPI data as:[9] $S = (d\ V_{pol}/dr)\ (L_{rad}/L_{pol})\ \tau_{auto}$, where $d\ V_{pol}/dr$ is the radial turbulence velocity gradient $|grad\ V_{pol}|$, L_{rad} and L_{pol} are the turbulence correlation lengths (FWHM) and τ_{auto} is the turbulence correlation time. Thus $S = 1$ occurs when the poloidal turbulence velocity gradient moves the turbulence structure over one radial correlation length by one poloidal correlation length in one autocorrelation time. The shot-averaged value of S can be estimated using the average radial gradient from Fig. 14(d) of $|grad\ V_{pol}| \sim 1.2 \pm 0.5$ km/s cm, along with turbulence results from a previous analysis of Ohmic plasmas at –2 cm inside the separatrix[28] of $L_{pol} \sim 5 \pm 2$ cm, $L_{rad} \sim 4.5 \pm 1.5$ and $\tau_{auto} \sim 14 \pm 3\ \mu s$, giving roughly $S = 1.5 \pm 1.0$. Interestingly, this average value of S is near $S \sim 1$. However, the large shot-to-shot variations in the magnitude of $|grad\ V_{pol}|$ from 0.34 to 1.9 km/s cm during 1 ms preceding the transition suggest that there is no single threshold in the turbulence decorrelation parameter S for the L-H transitions in this database.

Although the focus of this paper was on the edge turbulence velocity *preceding* the L-H transition and its correlation with the transition trigger mechanism, some results were also shown in Figs. 3, 8, 11, 12, and 13 for the time period up to 5 ms after the transition. As noted at the end of Sec. III C, there was a wide shot-to-shot variation in the time-averaged $\langle V_{pol}\rangle_{pol}$ from just before to just after the transition, with this velocity change ranging from –5 km/s to +5 km/s, and with a 16-shot average change of nearly zero. For example, in the first shot #138113 of Sec. III A, neither the $\langle V_{pol}\rangle_{pol}$ in Fig. 3 nor the standard deviations of $\langle V_{pol}\rangle_{pol}$ in Fig. 5 show any significant change from L-mode to H-mode at –2 cm, while in the second shot #141922

of Sec. III B both of these quantities show a significant increase from L-mode to H-mode at −2 cm, as shown in Figs. 8 and 10.

We interpret this wide variation as due at least partially to the varying radial location of the narrow pedestal gradient region with respect to the fixed GPI analysis location at −2 cm inside the separatrix. For example, the electron density pedestal width in NSTX for these shots just after the transition varies from ∼2–7 cm, and the middle of this electron density gradient region varies from ∼2–5 cm inside the separatrix. Thus a variable location of the narrow E_r well structure as seen in H-mode[4–8] will very likely affect the measured turbulence velocity and its gradient at the constant GPI analysis location, whereas the E_r profile in L-mode is much broader. A second issue is that the radial width of the GPI emission region narrows during H-mode, as shown in Figs. 1 and 6, making it difficult to evaluate the radial profile of $\langle V_{pol}\rangle_{pol}$ in H-mode. Finally, since the fluctuation level decreases significantly in H-mode, the cross correlation analysis of $\langle V_{pol}\rangle_{pol}$ is more uncertain (see the Appendix). Thus the observed changes in $\langle V_{pol}\rangle_{pol}$ from before to after the L-H transition are not well understood at present. A detailed analysis of these changes would certainly be interesting, but unfortunately is beyond the scope of this paper.

D. Conclusions

The goal of this paper was to look for clear and consistent changes in the poloidally turbulence velocity preceding the L-H transition in NSTX GPI data. Within the limitations and uncertainties described in Sec. IV B, this paper concludes that no such clear and consistent changes in the turbulence velocity were observed in a region where the relative fluctuation decreased significantly at the L-H transition, i.e., at −2 cm inside the separatrix.

Among the 16 shots in this database, there was a wide variation of the average poloidal velocity $\langle V_{pol}\rangle_{pol}$, the magnitude of the poloidal velocity $|V_{pol}|$, and the magnitude of the radial velocity gradient $|\text{grad } V_{pol}|$ preceding the L-H transition, implying that there was no single threshold in these quantities required for the transition. For example, during the 1 ms preceding the transition the average magnitude of the poloidal velocity ranged from 1 to 4 km/s and its radial-gradient magnitude ranged from 0.34 to 1.9 km/s cm, as shown in Fig. 14. As mentioned at the end of Sec. III E, it is not yet clear what causes these shot-to-shot variations of $|V_{pol}|$ and $|\text{grad } V_{pol}|$ in the present dataset.

The limited-time resolution of these measurements leaves open the possibility that a sudden velocity change faster than 50 μs might cause the transition. However, such velocity changes at the transition are not visible by eye in the GPI movies,[31] in which the turbulence just seems to turn off over about 100 μs (see the supplementary material).

The spectral analysis of the $\langle V_{pol}\rangle_{pol}$ as shown in Figs. 4, 9, and 11 and summarized in Fig. 15 showed that only about half of the shots in the database had low frequency (∼3–5 kHz) zonal flow oscillations in the 30 ms before the L-H transition. The time of the maximum poloidal velocity spectral amplitude in most shots was more than 4 ms before the transition, as shown in Fig. 15(a). Thus zonal flow oscillations were not necessary for the L-H transition in NSTX.

But what did trigger the L-H transitions in these NSTX shots? One possibility is that there were very rapid ($\leq$50 μs) and/or very small ($\leq$0.5 km/s) changes in the turbulence velocity or its radial gradient at the transition which were not detected by the present analysis. These changes might be identified using some alternative frame-by-frame analysis of the structure and motion of the turbulence during the ±100 μs period around the transition. A second possibility is that the instability causing the edge turbulence in L-mode is stabilized without any consistent changes in the local turbulence velocity. This could be explored using computational simulations to better understand the L-mode turbulence and its dependence on the edge plasma parameters.

SUPPLEMENTARY MATERIAL

See the supplementary material for videos of 3 ms of GPI data across the L-H transition for shots #138113, 141922, 141751, 142006, and 142229. Each shot plays for 1 min.

ACKNOWLEDGMENTS

We thank R. J. Maqueda and W. M. Davis for their long-term collaborations on the NSTX GPI diagnostic, W. W. Lee for helpful discussions, S. Sabbagh for the EFIT analysis, B. LeBlanc for the Thomson scattering data, and the NSTX/NSTX-Upgrade Team for their support for this work. This material is based upon work supported by the USDOE under Contract Nos. DE-AC02 09CH11466 and DE-SC0019302.

APPENDIX: GPIFLOW CODE

The GPIFLOW code calculates the poloidally averaged poloidal turbulence velocity in the GPI image data, which consists of 2D images with 64 × 80 pixels taken at 400,000 frames/s (see Sec. II A). This code is similar code those used previously for calculating poloidal flows in GPI data from NSTX[9] and Alcator C-Mod.[32] A comparison of this method with a Fourier velocity algorithm was given in Ref. 39.

The GPIFLOW algorithm is based on the intuitive idea that the turbulence flow speed can be estimated by cross-correlating a short time series from a given pixel in the 2D image with time-delayed time series at all neighboring pixels. The location of the maximum of the time-delayed cross correlation is used to determine the movement of the turbulence in the GPI image plane over the delay time. The 2-D velocity is evaluated from the displacement of the maximum of this time-delayed correlation divided by the delay time. The code assumes that the image rows vs columns are aligned in the poloidal vs radial direction (see Fig. 1). The normalized time delayed cross correlation function was evaluated using the "c_correlate" function in IDL. The image data were not smoothed in space or time before starting the analysis.

Several parameters in this cross correlation analysis were chosen to be appropriate for this NSTX data. The length of the cross-correlating time series was ±11 frames or ±27.5 μs long around each time point. This was long enough to produce a statistically significant correlation coefficient at a single pixel in a single frame, but short enough to allow the velocity to be estimated below ∼20 kHz, which included the ∼3 kHz velocity oscillation seen previously in NSTX GPI data.[9] The time delay over which the cross correlation was evaluated was 1 frame, which allowed the turbulence velocity at each pixel at each frame to be evaluated in units of 1 pixel/frame or 1.5 km/s. The search for the maximum of the time-delayed cross correlation was done over ±10 pixels in both directions, which allowed a maximum velocity of 15 km/s. The resulting

poloidal turbulence velocity was then averaged over 15 different pixels in each image column, where these pixels were spaced 4 rows (1.5 cm) apart between rows 10 and 66, allowing 10 rows at either end for the correlation search. The resulting poloidally turbulence velocity was averaged 21.5 cm in the poloidal direction in each column (i.e., at each radius). The resulting velocity at each pixel was averaged over ±6 frames (±15 μs) to reduce discreteness of the velocity derived at each individual frame.

The poloidally averaged poloidal velocities $\langle V_{\rm pol}\rangle_{\rm pol}$ in the 15 ms preceding the L-H transition in a column −2 cm inside the separatrix typically ranged up to ±6 km/s, as illustrated in Fig. 3(a). This corresponds to a poloidal displacement of up to ±4 pixels over the 1 frame delay time. The maximum value of this cross correlation coefficient found over a 1 frame delay for the 16 shots in L-mode ranged from 0.83 ± 0.06 to 0.95 ± 0.02. This correlation coefficient was high since the turbulence poloidal correlation lengths were ∼4 cm (10 pixels FWHM) and the autocorrelation times were ∼15 ms (6 frames HWHM).[26] Similar velocities were found using a 2 frame delay, but the larger search over ±20 pixels limited the poloidal averaging. The maximum cross correlation during the 1 ms period in H-mode just after the L-H transition varied from 0.67 ± 0.07 to 0.89 ± 0.07, which was lower due to the smaller turbulence level and lower signal/noise. This makes the velocity estimations in H-mode more uncertain.

A test of this code using a known turbulence velocity is shown in Fig. 16. Here a single frame from shot #138113 at 1 ms before the L-H transition is used as an initial condition, and this frame is forced to oscillate poloidally at a velocity of 1 pixel/frame (1.5 km/s) with a frequency of 2.5 kHz, as shown by the red line. The pixels which leave at the top (bottom) of the frame are put back at the bottom (top). The code result for a single column at a radius of −2 cm (black line) is exactly correct when the velocity is constant, but near the times of the sudden velocity reversal the code responds slowly over ±27.5 μs, which is the duration over which the cross correlation is evaluated at each time step. Thus when the velocity changes direction within the time over which the cross correlation is done, this code produces incorrect velocities.

It is important to note that the deviations from the correct velocity during these velocity reversal times are considerably larger and different from each other at each of the 15 individual pixels which were averaged to get the poloidally averaged result in Fig. 16. These individual pixel velocities varied over a range from +3 to −5 km/s within ±27.5 μs of the velocity reversal times due to the small-scale randomness of the image. By averaging 15 poloidal pixels (i.e., 21 cm poloidally) these incorrect velocities are considerably mitigated, as shown in Fig. 16.

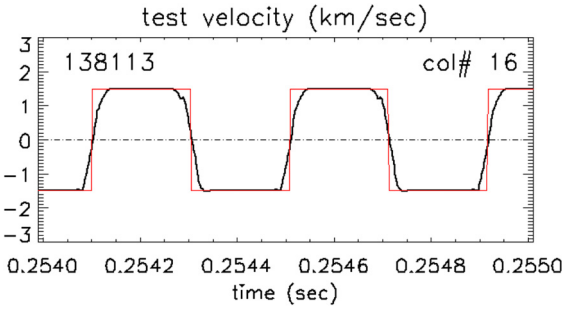

FIG. 16. Test of GPIFLOW code using an imposed square-wave velocity signal of 1 pixel/frame at a frequency of 2.5 kHz. The initial condition was the column at –2 cm from shot #138113 at 1 ms before the L-H transition. The code obtained the correct velocity of 1.5 km/s in steady-state (black), but had a response time of ±27.5 μs at each velocity reversal. The forcing velocity is in red.

The poloidally averaged results for initial conditions from other shots looked qualitatively similar to Fig. 16, with exactly correct results during the times of constant velocity but incorrect velocities during the velocity reversals. Similar results were obtained for a variety of random blob sizes and even for an image of 64 × 80 random numbers. The conclusion from these test cases was that the poloidally averaged GPIFLOW code could accurately detect large-scale poloidal flows which were frozen in space and varied slower than 20 kHz. However, the code gives inaccurate results for single pixels when the velocity changes more rapidly than the code's cross correlation time. Thus this code cannot be used to calculate Reynold's stresses, which require local velocities on a turbulence timescale.

It is useful to estimate the uncertainty in the poloidally averaged poloidal velocity results due to the small-scale turbulent motions which are always superimposed on the large-scale poloidal flows. The local turbulence characteristics were measured previously for Ohmic plasmas in NSTX at −2 cm inside the separatrix;[28] namely, the poloidal correlation length was ∼5 cm (FWHM), the autocorrelation time was ∼15 μs, and the time-averaged turbulence velocity was ∼2 km/s. Within the GPIFLOW correlation time of ±27.5 μs there are about 4 turbulence autocorrelation times, and within the poloidal averaging length of 21 cm there are about 4 turbulence correlation lengths. Assuming that these turbulent motions are random in the poloidal direction, the resulting net velocity within these averaging intervals can be estimated by a random walk in velocity to be $(1/\sqrt{4\times 4})\times 2$ km/s ∼0.5 km/s. We take this to be the rough uncertainty in a single measurement of the poloidally averaged poloidal velocity. It is difficult to be more precise since the local time-dependent turbulence velocities are not known.

DATA AVAILABILITY

The data that support the findings of this study are openly available in the PPPL Dataspace Archive at http://arks.princeton.edu/ark:/88435/dsp018p58pg29j, Ref. 49.

REFERENCES

[1]F. Wagner, Plasma Phys. Controlled Fusion **49**, B1 (2007).
[2]J. W. Connor and H. R. Wilson, Plasma Phys. Controlled Fusion **42**, R1 (2000).
[3]H. Biglari, P. H. Diamond, and P. W. Terry, Phys. Fluids B **2**, 1 (1990).
[4]G. R. Tynan, I. Cziegler, P. H. Diamond, M. Malkov, A. Hubbard, J. W. Hughes, J. L. Terry, and J. H. Irby, Plasma Phys. Controlled Fusion **58**, 044003 (2016).
[5]G. S. Xu and X. Wu, Plasma Sci. Technol. **19**, 033001 (2017).
[6]L. Schmitz, Nucl. Fusion **57**, 025003 (2017).
[7]T. Kobayashi, Nucl. Fusion **60**, 095001 (2020).
[8]K. H. Burrell, Phys. Plasmas **27**, 060501 (2020).
[9]S. J. Zweben, R. J. Maqueda, R. Hager, K. Hallatschek, S. M. Kaye, T. Munsat, F. M. Poli, A. L. Roquemore, Y. Sechrest, and D. P. Stotler, Phys. Plasmas **17**, 102502 (2010).
[10]A. Diallo, S. Banerjee, S. J. Zweben, and T. Stoltzfus-Dueck, Nucl. Fusion **57**, 066050 (2017).

[11]A. Fujisawa, Nucl. Fusion **49**, 013001 (2009).
[12]Z. Yan, G. R. McKee, R. Fonck, P. Gohil, R. J. Groebner, and T. H. Osborne, Phys. Rev. Lett. **112**, 125002 (2014).
[13]D. M. Kriete, G. R. McKee, L. Schmitz, D. R. Smith, Z. Yan, L. A. Morton, and R. J. Fonck, Phys. Plasmas **27**, 062507 (2020).
[14]L. M. Shao, G. S. Xu, S. C. Liu, S. J. Zweben, B. N. Wan, H. Y. Guo, A. D. Liu, R. Chen, B. Cao, W. Zhang, H. Q. Wang, L. Wang, S. Y. Ding, N. Yan, G. H. Hu, H. Xiong, L. Chen, Y. L. Liu, N. Zhao, and Y. L. Li, Plasma Phys. Controlled Fusion **55**, 105006 (2013).
[15]I. Cziegler, G. R. Tynan, P. H. Diamond, A. E. Hubbard, J. W. Hughes, J. Irby, and J. L. Terry, Plasma Phys. Controlled Fusion **56**, 075013 (2014).
[16]G. D. Conway, C. Angioni, F. Ryter, P. Sauter, J. Vicente, and ASDEX Upgrade Team, Phys. Rev. Lett. **106**, 065001 (2011).
[17]L. Schmitz, L. Zeng, T. L. Rhodes, J. C. Hillesheim, E. J. Doyle, R. J. Groebner, W. A. Peebles, K. H. Burrell, and G. Wang, Phys. Rev. Lett. **108**, 155002 (2012).
[18]G. Birkenmeier, M. Cavedon, G. D. Conway, P. Manz, U. Stroth, R. Fischer, G. Fuchert, T. Happel, F. M. Laggner, M. Maraschek, A. Medvedeva, V. Nikolaeva, D. Prisiazhniuk, T. Pütterich, F. Ryter, L. M. Shao, M. Willensdorfer, E. Wolfrum, H. Zohm, and ASDEX Upgrade Team, Nucl. Fusion **56**, 086009 (2016).
[19]J. C. Hillesheim, E. Delabie, H. Meyer, C. F. Maggi, L. Meneses, E. Poli, and JET Contributors, Phys. Rev. Lett. **116**, 065002 (2016).
[20]W. Zhong, X. Zou, Z. Shi, X. Duan, M. Xu, Z. Yang, P. Shi, M. Jiang, G. Xiao, X. Song, J. Dong, X. Ding, Y. Liu, and HL-2A Team, Plasma Sci. Technol. **19**, 070501 (2017).
[21]G. S. Xu, B. N. Wan, H. Q. Wang, H. Y. Guo, H. L. Zhao, A. D. Liu, V. Naulin, P. H. Diamond, G. R. Tynan, M. Xu, R. Chen, M. Jiang, P. Liu, N. Yan, W. Zhang, L. Wang, S. C. Liu, and S. Y. Ding, Phys. Rev. Lett. **107**, 125001 (2011).
[22]G. S. Xu, H. Q. Wang, M. Xu, B. N. Wan, H. Y. Guo, P. H. Diamond3, G. R. Tynan, R. Chen, N. Yan, D. F. Kong, H. L. Zhao, A. D. Liu, T. Lan, V. Naulin, A. H. Nielsen, J. Juul Rasmussen, K. Miki, P. Manz, W. Zhang, L. Wang, L. M. Shao, S. C. Liu, L. Chen, S. Y. Ding, N. Zhao, Y. L. Li, Y. L. Liu, G. H. Hu, X. Q. Wu, and X. Z. Gong, Nucl. Fusion **54**, 103002 (2014).
[23]L. M. Shao, G. S. Xu, R. Chen, L. Chen, G. Birkenmeier, Y. M. Duan, W. Gao, P. Manz, T. H. Shi, H. Q. Wang, L. Wang, M. Xu, N. Yan, L. Zhang, and EAST Team, Plasma Phys. Controlled Fusion **60**, 035012 (2018).
[24]J. Wu, T. Lan, G. Zhuang, M. Xu, C. X. Yu, J. R. Wu, L. Nie, W. Chen, L. M. Yu, J. Cheng, L. W. Yan, X. R. Duan, T. J. Deng, H. Q. Xu, S. Zhang, J. F. Zhu, Y. Yu, X. Sun, W. Z. Mao, A. D. Liu, J. L. Xie, H. Li, W. X. Ding, and W. D. Liu, Phys. Plasmas **27**, 012304 (2020).
[25]T. Estrada, C. Hidalgo, T. Happel, and P. H. Diamond, Phys. Rev. Lett. **107**, 245004 (2011).
[26]T. Kobayashi, U. Losada, B. Liu, T. Estrada, B. Ph. van Milligen, R. Gerrú, M. Sasaki, and C. Hidalgo, Nucl. Fusion **59**, 044006 (2019).
[27]S. J. Zweben, D. P. Stotler, F. Scotti, and J. R. Myra, Phys. Plasmas **24**, 102509 (2017).
[28]S. J. Zweben, W. M. Davis, S. M. Kaye, J. R. Myra, R. E. Bell, B. P. LeBlanc, R. J. Maqueda, T. Munsat, S. A. Sabbagh, Y. Sechrest, D. P. Stotler, and the NSTX Team, Nucl. Fusion **55**, 093035 (2015).
[29]S. J. Zweben, J. L. Terry, D. P. Stotler, and R. J. Maqueda, Rev. Sci. Instrum. **88**, 041101 (2017).
[30]S. J. Zweben, D. P. Stotler, R. Bell, W. M. Davis, S. M. Kaye, B. P. LeBlanc, R. J. Maqueda, E. T. Meier, T. Munsat, Y. Ren, S. A. Sabbagh, Y. Sechrest, D. R. Smith, and V. Soukhanovskii, Plasma Phys. Controlled Fusion **56**, 095010 (2014).
[31]Videos at https://w3.pppl.gov/~szweben/NSTX2013/NSTX2013.html.
[32]S. J. Zweben, J. L. Terry, M. Agostini, R. Hager, J. W. Hughes, J. R. Myra, D. C. Pace, and the Alcator C-Mod Group. Plasma Phys. Controlled Fusion **54**, 025008 (2012).
[33]T. Munsat and S. J. Zweben, Rev. Sci. Instrum. **77**, 103501 (2006).
[34]Y. Sechrest, T. Munsat, D. A. D'Ippolito, R. J. Maqueda, J. R. Myra, D. Russell, and S. J. Zweben, Phys. Plasmas **18**, 012502 (2011).
[35]S. Banerjee, H. Zushi, N. Nishino, K. Mishra, T. Onchi, A. Kuzmin, Y. Nagashima, K. Hanada, K. Nakamura, H. Idei, M. Hasegawa, and A. Fujisawa, Rev. Sci. Instrum. **86**, 033505 (2015).
[36]G. McKee, R. J. Fonck, D. K. Gupta, D. J. Schlossberg, and M. W. Shafer, Rev. Sci. Instrum. **75**, 3490 (2004).
[37]S. Zoletnik, L. Bardoczi, A. Kramer-Flecken, Y. Xu, I. Shesterikov, S. Soldatov, G. Anda, D. Dunai, G. Petravich, and TEXTOR Team. Plasma Phys. Controlled Fusion **54**, 065007 (2012).
[38]D. M. Kriete, G. R. McKee, R. J. Fonck, D. R. Smith, G. G. Whelan, and Z. Yan, Rev. Sci. Instrum. **89**, 10E107 (2018).
[39]J. M. Sierchio, I. Cziegler, J. L. Terry, A. E. White, and S. J. Zweben, Rev. Sci. Instrum. **87**, 023502 (2016).
[40]R. Maingi, C. E. Bush, E. D. Fredrickson, D. A. Gates, S. M. Kaye, B. P. LeBlanc, J. E. Menard, H. Meyer, D. Mueller, N. Nishino, A. L. Roquemore, S. A. Sabbagh, K. Tritz, S. J. Zweben, M. G. Bell, R. E. Bell, T. Biewer, J. A. Boedo, D. W. Johnson, R. Kaita, H. W. Kugel, R. J. Maqueda, T. Munsat, R. Raman, V. A. Soukhanovskii, T. Stevenson, and D. Stutman, Nucl. Fusion **45**, 1066 (2005).
[41]S. M. Kaye, R. Maingi, D. Battaglia, R. E. Bell, C. S. Chang, J. Hosea, H. Kugel, B. P. LeBlanc, H. Meyer, G. Y. Park, and J. R. Wilson, Nucl. Fusion **51**, 113019 (2011).
[42]B. Cao, D. P. Stotler, S. J. Zweben, M. Bell, A. Diallo, and B. LeBlanc, Fusion Sci. Technol. **64**, 29 (2013).
[43]S. Banerjee, A. Diallo, and S. J. Zweben, Phys. Plasmas **23**, 044502 (2016).
[44]B. Horn and B. G. Schnuck, Artif. Intell. **17**, 185 (1981).
[45]M. Cavedon, G. Birkenmeier, T. Pütterich, F. Ryter, E. Viezzer, E. Wolfrum, R. Dux, T. Happel, P. Hennequin, U. Plank, U. Stroth, M. Willensdorfer, and ASDEX Upgrade Team. Nucl. Fusion **60**, 066026 (2020).
[46]A. S. Liang, X. L. Zou, W. L. Zhong, A. Ekedahl, X. R. Duan, Z. B. Shi, D. L. Yu, Z. C. Yang, J. Wen, G. L. Xiao, M. K. Han, J. Li, X. R. Zhang, M. Jiang, P. W. Shi, K. R. Fang, X. X. He, W. Chen, X. M. Song, L. W. Yan, Y. Liu, Q. W. Yang, J. Q. Dong, X. T. Ding, and M. Xu, Nucl. Fusion **60**, 092002 (2020).
[47]L. M. Shao, G. S. Xu, N. Yan, R. Chen, L. Chen, Y. M. Duan, W. Gao, J. P. Qian, W. Shea, A. Ti, M. Xu, Q. Yu, L. Zhang, T. F. Zhou, and EAST Team. Phys. Lett. A **384**, 126184 (2020).
[48]D. A. D'Ippolito, J. R. Myra, and S. J. Zweben, Phys. Plasmas **18**, 060501 (2011).
[49]S. J. Zweben, A. Diallo, M. Lampert, T. Stoltfus-Dueck, and S. Banerjee, http://arks.princeton.edu/ark:/88435/dsp018p58pg29j for "Edge turbulence velocity preceding the L-H transition in NSTX," PPPL Dataspace Archive (2021).